Geologic modeling and fluid-flow simulation of acid gas disposal in western Wyoming

Shuiquan Li, Ye Zhang, Xu Zhang, and Changan Du

ABSTRACT

The Moxa arch anticline is a regional-scale northwest-trending uplift in western Wyoming where geologic storage of acid gas (carbon dioxide, methane, nitrogen, hydrogen sulfide, ethane) is under consideration. Nugget Sandstone, a deep saline aquifer at depths exceeding 17,000 ft (5180 m), is a candidate formation. This study builds three-dimensional local- to regional-scale geologic and fluid-flow models for the Nugget Sandstone and its neighboring formations. Geologic and engineering characterization data were assembled and screened for accuracy. Using geostatistical simulations (first, sequential indicator simulation of facies, then the sequential Gaussian simulation of porosity [ϕ]), the data were integrated to create a regional-scale geologic model from which a local-scale simulation model surrounding the proposed injection site was extracted. Using this model, acid gas injection was simulated for 50 yr, followed by 1950 yr of monitoring. A sensitivity analysis was conducted, exploring the impact of geologic and engineering variables on model predictions. Results suggest that, at the simulation time scale, low dissolved solids in formation water, large gas-phase relative permeability (k_{rg}) hysteresis, and low vertical-to-horizontal intrinsic permeability (k) anisotropy all contribute to enhanced storage of acid gas in both residual (trapped) and dissolved forms. The parameter that exerts the largest control on gas storage is relative permeability hysteresis. However, given parameter uncertainty, the total predicted gas storage

Manuscript received November 12, 2010; provisional acceptance January 17, 2011; revised manuscript received March 15, 2011; revised manuscript provisional acceptance June 16, 2011; second revised manuscript received July 12, 2011; final acceptance July 26, 2011.
DOI:10.1306/07261110178

AUTHORS

SHUIQUAN LI ~ *Department of Geology and Geophysics, University of Wyoming, 1000 East University Avenue, Laramie, Wyoming; sli2@uwyo.edu*

Shuiquan Li received his B.S. and M.S. degrees in petroleum engineering from Southwest Petroleum Institute, People's Republic of China (1985, 1988) and his Ph.D. in engineering mechanics from Tsinghua University, People's Republic of China (2000). He is currently a postdoctoral associate at the University of Wyoming. His research interests include reservoir modeling, geomechanics, reservoir characterization, flow simulation in deformable porous and fractured media, and carbon dioxide sequestration.

YE ZHANG ~ *Department of Geology and Geophysics, University of Wyoming, 1000 East University Avenue, Laramie, Wyoming; yzhang9@uwyo.edu*

Ye Zhang received her B.S. degree in hydrogeology and engineering geology from Nanjing University, People's Republic of China (1998); her M.S. degree in hydrogeology from the University of Minnesota (2004); and her Ph.D. in hydrogeology from Indiana University (2005). She is currently an assistant professor of geology at the University of Wyoming. Her research interests include geologic modeling, geostatistics, upscaling, and uncertainty analysis in subsurface-flow simulations.

XU ZHANG ~ *Schlumberger Information Solutions (SIS), Schlumberger, 5599 San Felipe, Suite 1700, Houston, Texas; xzhang6@slb.com*

Xu Zhang received his B.S. degree (1982) in petroleum engineering from the Southwestern Petroleum Institute, People's Republic of China; and his M.S. degree (1990) and Ph.D. (1994), both in petroleum engineering, from the University of Oklahoma. He is currently a senior reservoir engineer at Schlumberger. His technical interests include reservoir simulation and management, and enhanced oil recovery techniques.

CHANGAN DU ~ *Schlumberger Information Solutions (SIS), Schlumberger, 14131 Midway Road, Suite 700, Addison, Texas; cdu2@slb.com*

Changan Du received his B.S. degree from Yangtze University, People's Republic of China (1983), M.S. degree from the Graduate School

of Research Institute of Petroleum Exploration and Development, China National Petroleum Corporation (1986), and Ph.D. from the University of Southern California (1996), all in petroleum engineering. His research interests include integrated reservoir characterization and modeling, reservoir engineering analysis and flow simulations, reservoir stimulations, and unconventional (shale gas) reservoir modeling and simulation studies.

ACKNOWLEDGEMENTS

This material is partially based on work supported by the Department of Energy National Energy Technology Laboratory under award number DE-NT0004730. Funding for this study was also provided by the School of Energy Resources at the University of Wyoming. The views of the authors do not reflect those of the agencies. We acknowledge the generous donation of software (Petrel, Petrophysics Interactive, Eclipse) from Schlumberger, Inc. The manuscript has benefited significantly from the suggestions and comments made by anonymous reviewers.

The AAPG Editor thanks the three anonymous reviewers for their work on this paper.

EDITOR'S NOTE

A color version of Figure 6 may be seen in the online version of this article.

varies significantly. Prediction uncertainty increases in the order of dissolved gas, trapped gas, and mobile gas. In comparison, petrophysical uncertainty, as represented by multiple ϕ realizations, has limited impact on prediction, although future work is needed to expand the uncertainty analysis by developing alternative facies models for the storage formations.

INTRODUCTION

The Moxa arch anticline is a northwest-trending basement-cored uplift in western Wyoming that formed during the Late Cretaceous (Figure 1). Natural gas is produced from the deeply buried Madison Limestone located at the crest of the anticline. The produced gas contains carbon dioxide (CO_2), methane (CH_4), nitrogen (N_2), hydrogen sulfide (H_2S), and helium (He). In 2005, a part of the produced CO_2 and all of the H_2S were injected into the Madison Limestone below a depth of 18,000 ft (5486 m), at the Shute Creek gas plant south of the producing field (La Barge platform). Since that time, more than 2 million tons of mixed gas have been sequestered. As the gas contains H_2S, this deep injection qualifies as acid gas disposal.

The University of Wyoming, in collaboration with industry, is evaluating the potential for expanded gas disposal in the Moxa arch. Candidate geologic formations include the Nugget Sandstone, Tensleep Sandstone, and Bighorn Dolomite, all saline aquifers lying at depths exceeding 13,000 ft (3960 m) and containing brine with more than 10,000 ppm total dissolved solids (TDS). Within the 12 townships surrounding Shute Creek, only 31 wells penetrate these formations, minimizing leakage risk via wellbores. At depth, natural CO_2 exists in the Madison and Bighorn formations, suggesting that adequate seals and hydrogeologic isolation exist (Huang et al., 2007; Lynds et al., 2010). As part of a larger goal of determining the suitability of these formations for gas disposal, this study conducts a numerical scoping analysis by building reservoir models and conducting gas injection simulations in the Nugget Sandstone, its overlying Twin Creek Formation, and its underlying Ankareh Formation, or together, the Nugget storage suite (NSS). Throughout the article, "Nugget" refers to the Nugget Sandstone. The Twin Creek and Ankareh formations are included in the storage model because low-permeability units exist above the Twin Creek and within the lower Ankareh. Gas injected into the Nugget will migrate into these formations before encountering significant flow barriers.

In the Moxa arch, the NSS is a deep saline aquifer for which reservoir characterization data are limited. Significant uncertainty

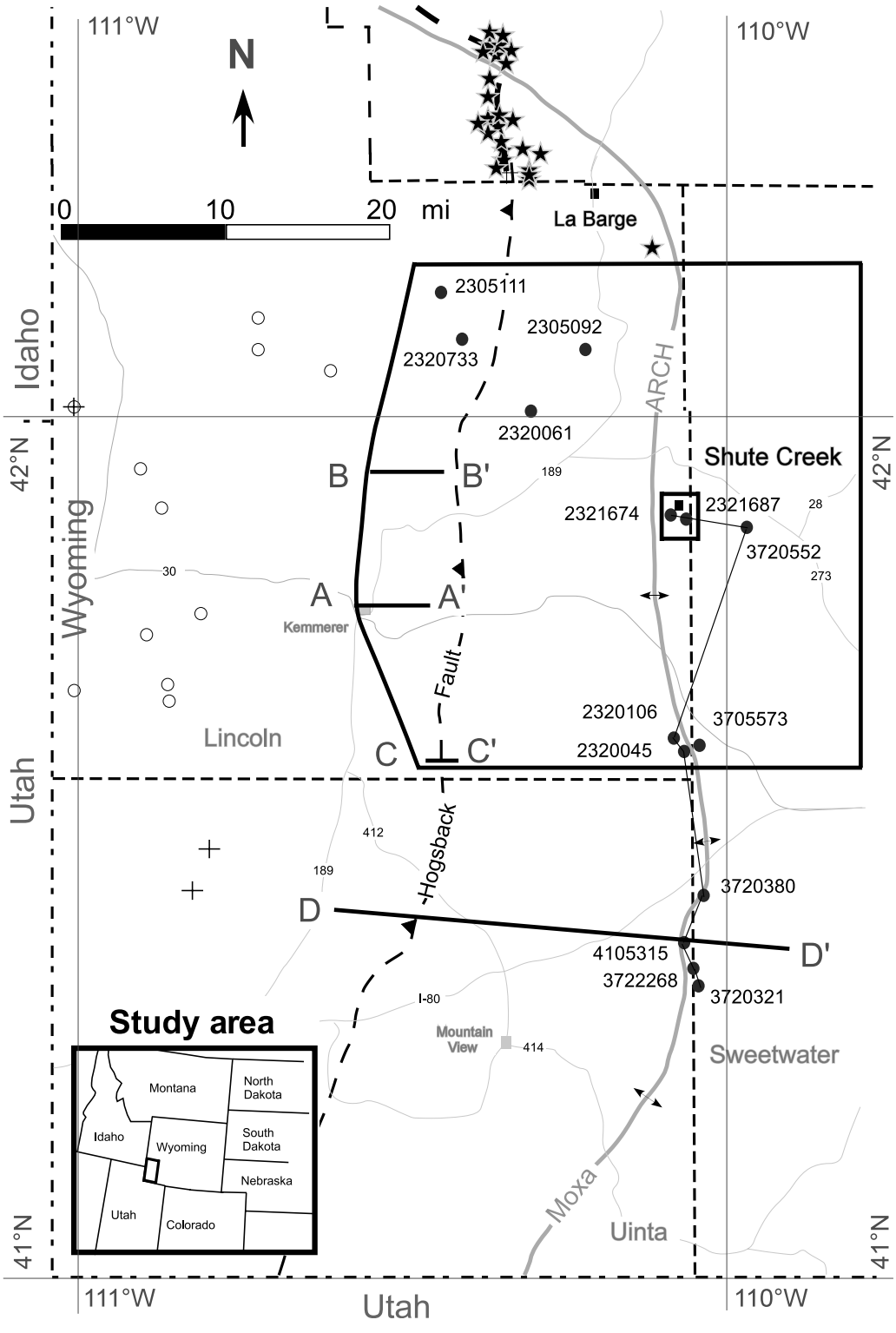

Figure 1. Moxa arch anticline in western Wyoming. The bold outline indicates the extent of a regional model (left side is the subsurface extent of the Nugget storage suite against Hogsback). An inner box centered at Shute Creek indicates the location of a local model. Subsets of the well database are shown: 14 wells in the Moxa arch (solid circles with API numbers); 11 wells in the overthrust belt (empty circles); 26 wells northwest of La Barge (stars), and 4 wells with core data (cross). Five other wells also have core data, but they are located outside the map area: four are farther north of La Barge; one is at Rock Spring uplift to the east. Locations of cross sections used for model building are also shown. DD′ and four wells south of the regional model were used in correlating formation tops, although they were cropped from the final model.

exists in building the geologic model and conducting fluid-flow simulation. This study identifies several sources of parameter uncertainty that can be constrained by the available data. By simulating gas injection at Shute Creek, the impact of these uncertainties on gas prediction is assessed. In the simulations, gas dissolution in brine is considered, as well as its partitioning between mobile and trapped gases (herein, "gas" refers to the combination of all gas-phase components). Driven by

buoyancy, mobile gas can migrate away from the injection site, thus, "gas storage" is defined as the total trapped and dissolved gas in the reservoir. Simulations predicting higher percentages of gas in trapped and dissolved forms are considered to be of higher storage security.

In the remainder of the text, geologic formations of the NSS are described, followed by a description of the data used to build the models. The model-building procedure is presented, leading to the creation of a high-resolution geostatistical grid. Multiple porosity (ϕ) realizations are created from which three models corresponding to P10, P50, and P90 pore volumes (PVs) are selected (the P10 model is one whose PV is higher than the PVs of 10% of the realizations). An upscaling analysis is conducted using multiple grid sizes until a coarsened flow grid is obtained with which acid gas injection is simulated. Within the framework of a sensitivity analysis, results of the simulations are presented.

GEOLOGIC FORMATIONS

The Moxa arch anticline is bounded to the west by the Wyoming-Utah overthrust belt, to the south by the Uinta Mountains in Utah, and to the north by the La Barge platform (Figures 1, 2). It transitions into the greater Green River Basin (GRB) to the east. The flanks of the Moxa arch are gently dipping, with an angle typically less than 3° (Royse, 1993). Geologic formations range from Precambrian crystalline rocks to alluvial sands and gravels deposited in the Holocene. Formations of interest in this study are the Jurassic Nugget Sandstone, the overlying Jurassic Twin Creek Formation, and the underlying Upper Triassic Ankareh Formation.

The Nugget Sandstone is primarily an eolian deposit with a lithology dominated by sandstone that has minor siltstone, mudstone, and limestone (Picard, 1975). In the Moxa arch, the Nugget has an average thickness of approximately 800 ft (~244 m) and lies at depths as great as 18,000 ft (5490 m) (Pacht, 1977; Picard, 1977; Spangler, 2007). It is a saline aquifer with TDS ranging from 10,000 to 115,000 ppm (Wyoming Oil Gas Conservation Commission, 2009). The Nugget Formation water is dominated by sodium chloride (NaCl) brines. Porosity in this formation averages approximately 12%, and k ranges from 0.1 to 1000 md. In western Wyoming, the Nugget Sandstone contains cross-bedded to low-angle, or horizontally bedded, fine-to-coarse sands deposited in dune and interdune environments (Lindquist, 1983). Two lithofacies were distinguished (Picard, 1975): a lower thinly bedded clay-rich deposit and an upper cross-stratified sand-rich deposit. Regional paleocurrent studies suggest that Nugget facies are commonly aligned northeast (Picard, 1975), locally ranging from N20E to N70E (Doelger, 1987).

Limited Nugget core data exist in the areas west (overthrust belt), north (north of La Barge), and east (Rock Spring uplift) of the Moxa arch (Figure 1). A few cores have reported fractures (Wyoming Oil Gas Conservation Commission, 2009; Frost, 2011), although their subsurface existence cannot be ascertained, nor it is clear whether fractures observed in cores exist in situ (image logs, e.g., Formation MicroImager, would be needed to distinguish between in-situ and drilling induced ones; Lorenz, 1995). In the overthrust belt, at Anschutz Ranch East field, the Nugget is observed to have experienced significant structural overprint. Here, core analyses suggest that primary Nugget ϕ and k (influenced by grain size, sorting, and bedding characteristics) have been modified by compaction, cementation, dissolution, and emplacement of organic matters (Lindquist, 1983; Cox et al., 1994). Both open and gouge-filled fractures are also observed here, with widely varying strike orientations, whereas fracture dip is dominated by high angles approaching vertical. In these neighboring regions, the k of Nugget cores exhibits a range of anisotropy, suggesting the existence of both open and closed (or no) fractures, although other mechanisms may also contribute, for example, cross-bedding, cementation, and deformation bands (Lewis and Couples, 1993; Morad et al., 2010). Subsurface stress conditions in the Moxa arch may differ from those of the neighboring regions; however, many of Wyoming's sandstone reservoirs are known to be fractured. Because fractures can become important to fluid flow when their density is high (forming an

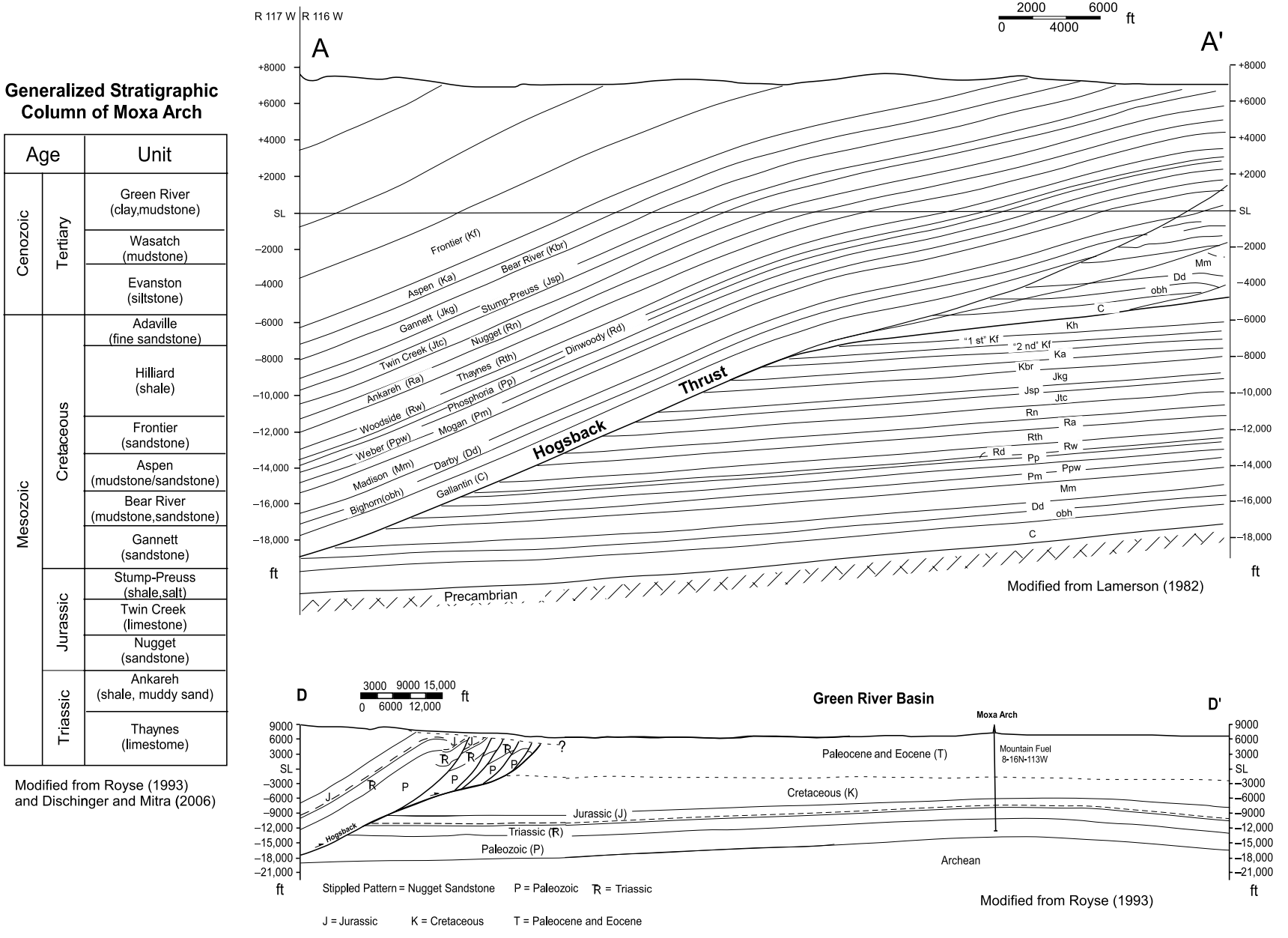

Figure 2. Stratigraphic column of the Nugget storage suite and overlying formations in the Moxa arch. Cross sections AA′ and DD′ are shown (Figure 1). In DD′, the top of the Nugget is marked by the dashed lines in the Jurassic (J) section. Modified from Lamerson, 1982; Royse, 1993; Dischinger and Mitra, 2006. SL = sea level.

interconnected network as fluid barriers or pathways depending on how connected and how open they are) and because high vertical fracture permeability (k_v) may contribute to gas leakage, this uncertainty is accounted for in building the geologic model, which is then propagated into gas injection simulations.

The Twin Creek Formation, which overlies the Nugget, is a shallow-marine shaly limestone, limy siltstone, and claystone (Love and Christiansen, 1985). Anhydrites exist locally in the basal Twin Creek, whereas overlying this formation is the Stump-Preuss shale composed of sandy siltstone, claystone, salts, sandstone, and limestone (Figure 2). At the Moxa arch, the Stump-Pruess shale locally contains sandstones with minor limestones (Imlay, 1950; Peterson, 1955; Jensen, 2005). Although this may pose a leakage risk for gas injected at Shute Creek, the overlying Gannett Group and Bear River and Aspen formations all contain significant low-permeability units that can provide additional seals (Hilman, 1973; Knapp, 1978; George, 1979; Doelger, 1987). Above the Frontier Sandstone (which overlies the Aspen) is the Hilliard Shale, a known sealing unit trapping Frontier gas (Harstad et al., 1996). The Ankareh Formation, which underlies the Nugget, is composed of interbedded mudstones, shale, siltstone, sandstone, and conglomerates (Love and Christiansen, 1985; Dischinger and Mitra, 2006). In parts of Utah, the Ankareh Formation was deposited in a supratidal environment with frequent subaerial exposures (Brandley, 1988). At the Moxa arch, the lower part of the Ankareh Formation is clay rich (as interpreted from limited logs), potentially acting as a flow barrier for the injected gas in the Nugget.

At the Moxa arch, limited information exists on leakage risk from faults. Based on data from a few wells, Krystinik (2000) discussed fractures and faults in Upper Cretaceous and shallower formations in the GRB. Wilkins (2007) discussed faults from the Upper Cretaceous down to the basement in an area east of the Moxa arch in the northern GRB. Recently, three-dimensional (3-D) seismic interpretations have been made at a location approximately 23,000 ft (~7000 m) northwest of Shute Creek (Frost, 2011). The seismic data cover an area of approximately 16,400 × 26,250 ft (5000 × 8000 m), extending from the surface down to the basement. Within the seismic resolution, the NSS and its overburden (northwest of Shute Creek) are not faulted, indicating small fault-related leakage risk in the areas surveyed (Frost, 2011).

METHODOLOGY

Data and Interpretations

A regional geologic model is built for the NSS using public-domain characterization data: (1) wireline logs from 165 wells that penetrate the Nugget Sandstone (Wyoming Oil Gas Conservation Commission, 2009); (2) core ϕ and k measurements from nine wells (API: 2320226, 3505128, 3520218, 3720642, 3722327, 3722344, 3920018, 4120083, 4120588); (3) four geologic cross sections (Lamerson, 1982; Royse, 1993) (Figure 1); and (4) three regional isopach maps, one for each NSS formation (MacLachlan, 1972; Peterson, 1972; Fraley, 1998). Well logs provide most of the data (Figure 1): 14 wells are located in the Moxa arch and the rest are located in neighboring regions. Many of the non–Moxa arch wells are located in the overthrust belt between the surface trace of the Hogsback thrust fault and the Idaho-Utah border. Only subsets of these wells are shown in Figure 1. The Nugget in the overthrust belt is a prolific gas and condensate producer (Lindquist, 1983), explaining the more abundant data there. At the Moxa arch, however, it is a deep saline aquifer with more limited and commonly incomplete data.

Before building the Moxa arch model, it was not known where in the subsurface NSS terminates against the Hogsback fault. All wells, supplemented by geologic cross sections, were needed to understand this relation. The cross sections (i.e., AA′, BB′, CC′, DD′, Figure 1) map out the western Moxa arch and parts of the overthrust belt (Figure 2). After careful screening of all data, two wells lying between the Hogsback trace and the Idaho-Utah border (API: 2305111, 2320733) were identified as penetrating the Moxa arch, whereas most of the overthrust belt wells penetrate the

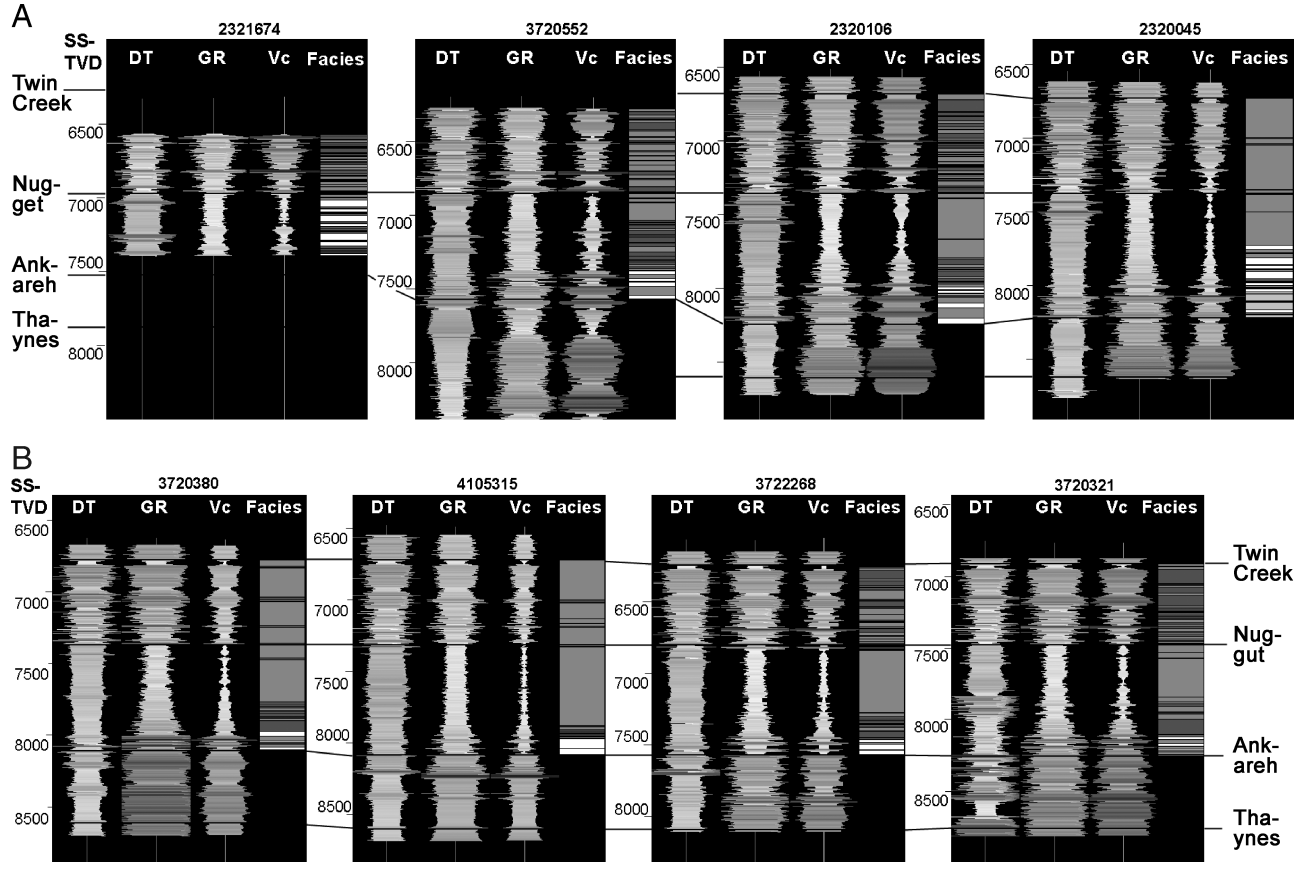

Figure 3. Formation correlation for the Nugget storage suite along a subset of the Moxa arch wells (north-south–oriented thin line; Figure 1). The top of the Nugget is the baseline. Panel B continues from A: those in A are located within the regional model, those in B are located south of the regional model. Data under Facies are petrofacies units, whereas the different gray scales stand for different petrofacies units. SSTVD = subsea true vertical depth; DT = sonic log; GR = gamma ray; V_c = computed clay volume of formation.

Nugget in the hanging walls of Hogsback and other faults. Moreover, each well has on average four to five logs, for example, density, gamma ray (GR), sonic (DT), neutron log, and less commonly, lithology and deviated survey logs. Thus, more than 900 logs were digitized. The logs were first screened for accuracy (those with inconsistent depth or incorrect datum information were removed) from which subsets were used for various interpretation tasks, as described below.

The 14 Moxa arch wells are used, along with cross sections and isopach data, for interpreting a regional NSS structure, that is, formation contacts (see Formation Structural Modeling section). A correlation chart (Figure 3) is built along a north-south transect (Figure 1). At each well, log signals are plotted against subsea true vertical depth. The columns are DT, GR, computed formation clay volume (V_c), and a computed petrofacies log (details on this are introduced later). Along this transect, the Nugget top rises gently toward the north, whereas its thickness does not change significantly. Within the extent of the structural model (bold outline in Figure 1 corresponding to panel A of Figure 3), a higher V_c is observed in the lower Nugget than in the upper Nugget, consistent with what is observed in the overthrust belt. The change in V_c is used to divide this formation into an upper sand-rich zone and a lower clay-rich zone. Within each zone, petrofacies modeling is conducted separately.

For these same 14 wells, logs are also interpreted to obtain estimates, at each well, of formation fluid type and saturation content. Data such as spontaneous potential, resistivity, and production records indicate that in most of the Moxa arch, Nugget Formation fluid is dominated by NaCl brines. At some wells, temperature measurements

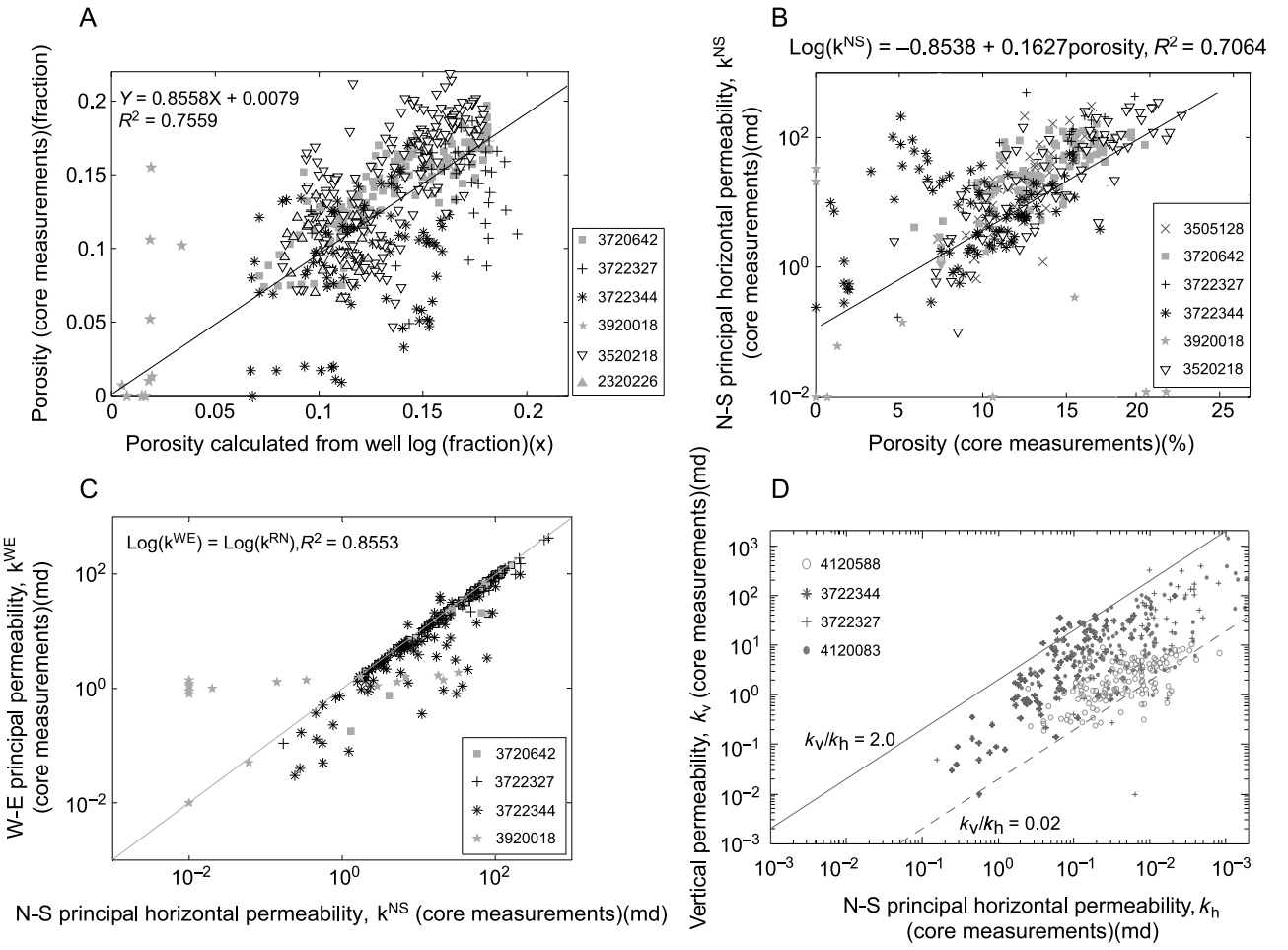

Figure 4. Nugget Sandstone core data. (A) Core porosity versus well-log–derived porosity. A linear correction function is fitted. Well API is shown. (B) North-south principal horizontal permeability versus porosity. A semilog transform is fitted. (C) North-south versus west-east horizontal permeability (line shown is a 1:1 line, not a fitting line). (D) Vertical permeability (k_v) versus north-south horizontal permeability. Two anisotropy ratios are fitted. k_h = horizontal permeability.

exist. These data are used to provide estimates of formation temperature and its vertical gradient based on which an initial temperature field is assigned to the model.

Well logs in the overthrust belt, besides providing information on the position of the NSS in relation to Hogsback and other faults, provide facies and petrophysical data for the Moxa arch model (Figure 1). These data are thus considered analogs, an acceptable practice when models are developed for data-poor reservoirs (Milliken et al., 2008). For example, a subset of 11 overthrust wells with appropriate log suites that can be used to distinguish facies is selected to provide supplemental information for facies variogram modeling. Another subset of 26 wells northwest of La Barge provides well-log–derived ϕ. Another nine wells provide core data: four in the overthrust belt are shown in Figure 1, the other five are located outside the map area (four north of La Barge, one near the Rock Spring uplift). At the 14 Moxa arch wells, neither core measurements nor physical rock specimens are available.

Core measurements provide direct information on petrophysical properties. They can be used to populate reservoir models and to calibrate well logs when both types of data exist. For the Nugget, well-log–derived porosity (ϕ_{well}) is calibrated against core measurements (ϕ_{core}) at the same well to obtain a linear calibration function (Figure 4A). Because the former involves assumptions on clay content and fitting coefficients in the petrophysical

equations (between well logs and ϕ_{well}), core measurements are considered more reliable. The fitted function in Figure 4A deviates slightly from 1:1, indicating a small bias. This function is used to calibrate ϕ_{well} at locations with no core measurements. The calibration will not remove the scatter in ϕ_{well}, instead, the bias between core and log measurements will be removed. All the calibrated ϕ_{well} are pooled together, and after appropriate scaling, are used in ϕ variogram modeling.

A semilog transform between ϕ_{core} and horizontal (north-south) permeability (k_h) is obtained for the Nugget (Figure 4B). The transform is used to populate k_h from a geostatistical ϕ model. Alternative transforms exist in developing ϕ-$\log_{10}k$ relations (e.g., cloud transform, cokriging), although they are not used. In a scoping study analyzing a data-poor reservoir, the simplest transform based on the available data is commonly preferred to facilitate understanding of petrophysical relations on flow predictions (Milliken et al., 2008). From the core data, Nugget k is nearly isotropic in the horizontal plane (Figure 4C) but exhibits a range of anisotropy in the vertical direction (Figure 4D). Two functions can be fitted to obtain a vertical-to-horizontal anisotropy ratio (k_v/k_h) of 2.0 and 0.02, with two orders of magnitude variation. The k_v/k_h = 2.0 may reflect vertical open fractures, whereas a value of 0.02 may reflect matrix anisotropy and/or bedding structures (Nelson, 2001). The higher value, although observed at core scale, if it belongs to a fracture network, can contribute to upward gas migration. The lower value represents closed, cemented, or no fractures. However, no rock specimens can be located at these wells for visual confirmation. This uncertainty will be accounted for in a parameter sensitivity analysis: k_v/k_h will be varied as an uncertain input parameter of the model. Specifically, multiple ratios will be assigned to a geostatistical grid to obtain a local k_v from a local k_h. This grid will in turn be upscaled to a simulation grid, thus, the effect of this uncertainty on gas prediction will be assessed.

At the nine wells with core measurements (all located outside the Moxa arch), data are too incomplete to develop a lithofacies model, which requires a simultaneous consideration of core data, well logs, and descriptions of rock specimens. The core data thus cannot be divided into facies-specific subgroups that can be used to develop facies-specific petrophysical relations. Instead, the relations are developed for the entire Nugget Sandstone, introducing uncertainty. To address this uncertainty, either a detailed facies study or history-matching exercise is needed (i.e., near-wellbore petrophysical relations can be calibrated based on well-test data). Both analyses cannot be supported by current data. Moreover, for the Twin Creek and the Ankareh formations, both nonproducers in the study area, public-domain core measurements of significant lengths do not exist. Porosity models for these formations are populated using ϕ_{well}, which thus cannot be calibrated. Permeability models for these formations are borrowed from the ϕ-$\log_{10}k$ transform developed for the Nugget. The k of the Twin Creek and the Ankareh formations is thus solely controlled by their respective ϕ distributions. Permeability is also assumed to be isotropic in the horizontal plane, whereas the same k_v/k_h is varied, assuming that fractures (if they exist) extend from Nugget into these formations. These assumptions and modeling choices constitute additional uncertainty, which cannot be constrained by data, although at the burial depth of the NSS, petrophysical properties of the formations may be impacted significantly by compaction and cementation, in addition to lithology-controlled variations (Beaumont and Foster, 1987; Lander and Walderhaug, 1999).

Geologic Modeling

The NSS, including the Twin Creek Formation, the Nugget Sandstone, and the Ankareh Formation, is considered a single storage unit (only the Nugget is the proposed injection interval). All three formations are heterogeneous, which will be modeled using a hierarchical workflow starting from modeling formation structure, to within-formation facies, and finally to within-facies petrophysical properties (McLennan and Deutsch, 2006). Because the NSS at the Moxa arch has limited data, analog approaches are adopted to facilitate facies and petrophysical modeling, which is considered appropriate for a scoping study: limited direct data are combined and

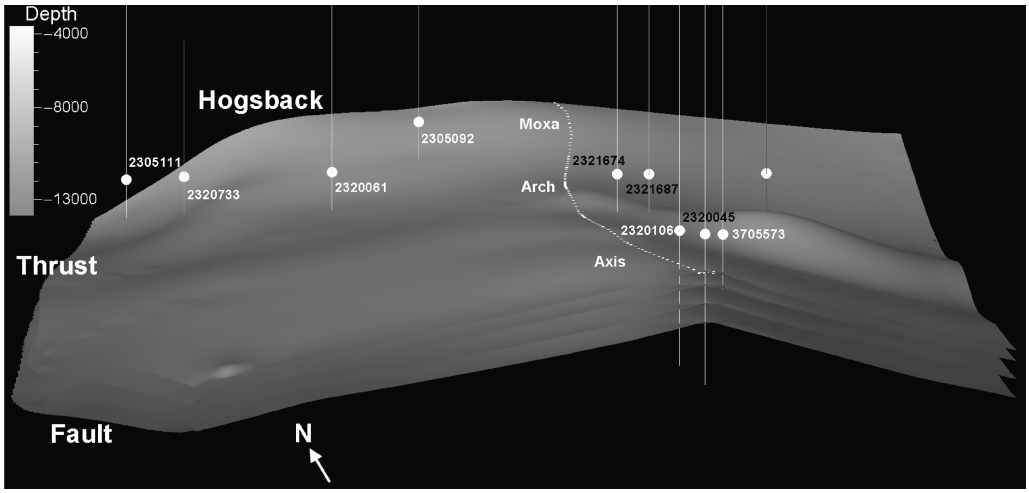

Figure 5. Regional structure model of the Nugget storage suite. The Moxa arch Axis is superimposed. Depth is subsea level in feet. The location of this model is indicated in Figure 1. The model uses 5× vertical exaggeration. The arrow points north.

supplemented by analog data to provide input to creating a geologic model. The results will help us develop a preliminary understanding of parameter and model uncertainty and their impact on prediction, thus providing a guide for future characterization efforts targeting specific uncertainties. This modeling philosophy is reflected by a multiyear study of a large gas reservoir, where four generations of geomodels were developed and refined over time as relevant data became available (Dubois et al., 2006).

Formation Structural Modeling

Well logs, cross sections, and isopach maps at the Moxa arch were integrated at the regional scale to obtain formation horizons for the NSS: Twin Creek top, Nugget top, Ankareh top, and Ankareh bottom (Figure 5). The horizons are truncated to the west by the Hogsback fault (its surface expression is shown in Figure 1). In creating the horizons, cross sections and isopach maps were digitized and control points were chosen along formation contacts. The control points were used as markers, along with formation tops picked from logs, to constrain the horizons. (To minimize extrapolation error, cross section DD′ along with four wells south of the structural model were used to create the horizons at a larger scale, before they were truncated by the structural model; Figure 1). In regions with sparse data (either well logs or markers), formation thickness was interpolated, allowing for physically correct extrapolation of contacts throughout the model region. The horizons were compared with two-dimensional seismic line shots in the southern Moxa arch (David et al., 1975; Royse et al., 1975). One seismic line lies approximately parallel to the arch axis and another lies perpendicular to it. Compared with these seismic profiles, the horizons exhibit correct formation thickness and continuity at the regional scale. Based on the horizons, a 3-D structural model of the NSS was built, spanning an average thickness of approximately 1700 ft (~520 m).

Facies Modeling

Petrophysical properties commonly vary by facies (Bahar and Mohan, 1997, 2004), thus, facies modeling is essential for the determination of reservoir versus nonreservoir quality units within a geologic formation. In this study, a distinction is made between lithofacies, which is linked to sediment physical characteristics (e.g., grain size, sorting, and primary and secondary sedimentary structures), and petrofacies, which is linked to sediment properties influencing flow (i.e., ϕ and k). Typically, many lithofacies can be distinguished within a reservoir, but different lithofacies can have overlapping petrophysical properties (Melick and Gardner, 2009). For ϕ and k modeling, petrofacies is more relevant. Because lithofacies can be grouped into petrofacies based on similar ϕ ranges, petrofacies are sometimes referred to as composite facies (Ma et al., 2009). Within the NSS, petrofacies were first categorized using well logs that indicate the existence

of distinct ϕ populations (Figure 3), before being verified against independent lithology logs, and then populated in the interwell region using geostatistics ("facies" now denotes petrofacies).

For the 14 Moxa arch wells and 11 facies analog wells of the overthrust belt, facies were categorized with Gaussian hierarchical clustering (GHC), a computationally efficient categorization algorithm (Fraley, 1998). At each well, GHC integrates and converts multiple continuous log signals (e.g., bulk density, GR, DT, neutron porosity log) to discrete facies types. Using well-log intervals within Twin Creek, three facies were identified (facies ID = 0–2). For the Nugget, based on the computed V_c, an upper sand-rich zone was manually divided from a lower clay-rich zone, which ensures that a later geostatistical population of facies can better satisfy stationarity. Using log intervals within each zone, six Nugget facies were categorized: three for the upper zone (ID = 3–5) and three for the lower zone (ID = 6–8). Compared to the Twin Creek and the Nugget, the Ankareh Formation has poorer reservoir quality and fewer logs, preventing direct application of GHC. No facies types can thus be identified for this formation, although from V_c of the few wells that logged this interval (Figure 3), a lower clay-rich region is observed. Ankareh is divided manually into a lower interval (ID = 11) and two upper intervals of equal thickness (ID = 9–10).

The above analysis was corroborated by conducting an independent neural network analysis using the same well logs (Schlumberger, 2010b). Results from the two methods are consistent. The computed petrofacies are also compared with independent lithofacies descriptions from mud logs (Wyoming Oil Gas Conservation Commission, 2009). Lithofacies were observed from rock cuttings obtained at increasing drilling depths where a geologist's observation is coded into a lithology log, reflecting a dominant lithofacies at that depth. At well 3722268 (Figure 1), for example, along most of the logged interval, the two types of facies are in agreement (Figure 6), although petrofacies (ϕ grouping) has a lower resolution than lithofacies (rock type), as expected. Discrepancy can be explained also by the fact that lithofacies do not always correspond to petrofacies because of the effect of diagenesis and finely interbedded sediments (Weber and van Guens, 1990). Overall, the comparison supports the petrofacies categorization. Finally, three facies modeling groups are created, capturing nonstationarity both within and across individual formations: (1) Twin Creek (three facies), (2) upper Nugget (three facies), and (3) lower Nugget (three facies). Based on well data within each group, proportions of the facies units were estimated (which add up to 1.0), creating a vertical proportion curve (VPC) of each facies.

Using petrofacies types categorized at wells, geostatistics can populate the facies spatially, with the requirement that facies be conditioned by well data while honoring global and local facies proportions. For each facies group, this is accomplished by two steps. (1) For each facies type, experimental facies variograms were constructed in the horizontal and vertical directions. Because no significant trends were observed in these variograms, stationary spherical models were fitted. To model horizontal anisotropy, N40E was selected to be the major azimuth angle, reflecting the mean angle of deposition. Given the limited Moxa arch wells, more data exist for computing vertical variograms than for horizontal variograms, many of which exhibit poor structures. Thus, analog wells from the overthrust belt were subject to the same facies categorization and variogram analyses, from which horizontal correlation ranges were obtained. These ranges were used to guide the fitting of horizontal facies variograms at the Moxa arch (Gringarten and Deutsch, 1999). Without such analogs, this fitting can be arbitrary and commonly suffers artifacts if automatic algorithms are used (Dubois et al., 2006). (2) Based on the fitted variogram models and estimated facies proportions, sequential indicator simulation (SIS) was conducted to populate facies within each group (Deutsch and Journel, 1998). Sequential indicator simulation honors the well data while creating multiple realizations to capture global facies proportions within each facies group and the VPC. One realization, considered equally likely as the next, was selected for the subsequent analysis. As mean ϕ of each facies is known from well logs, all realizations yield approximately the same total reservoir PV.

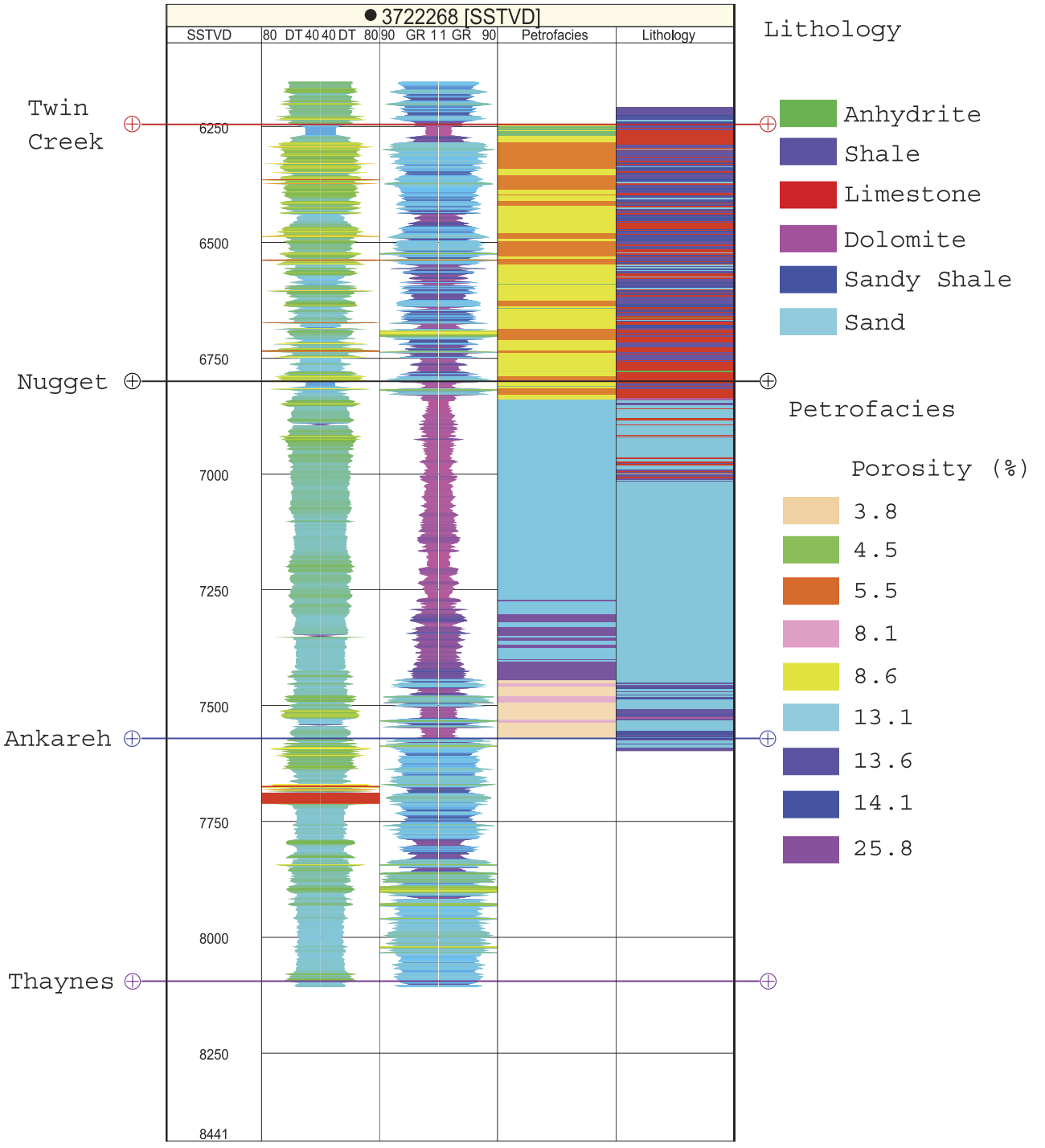

Figure 6. Predicted petrofacies versus a lithology log at well 3722268 (Figure 1). Mean porosity (%) for each petrofacies is computed from averaging ϕ_{well} (each petrofacies is linked to an underlying porosity distribution). Lithology types are also shown. SSTVD = subsea true vertical depth; DT = sonic log; GR = gamma ray. See online version for a color version of this figure.

A 12-unit model is created for the NSS (nine Nugget and Twin Creek facies and three Ankareh intervals), containing 35,385,840 grid cells with an average vertical grid spacing of 25 ft (7.6 m) (Figure 7). The model captures both the east-west arch structure and the north-south upward incline. In Nugget and Twin Creek, because of the anisotropy modeled in the directional facies variograms (i.e., horizontal range typically two orders of magnitude larger than vertical range), the facies' vertical

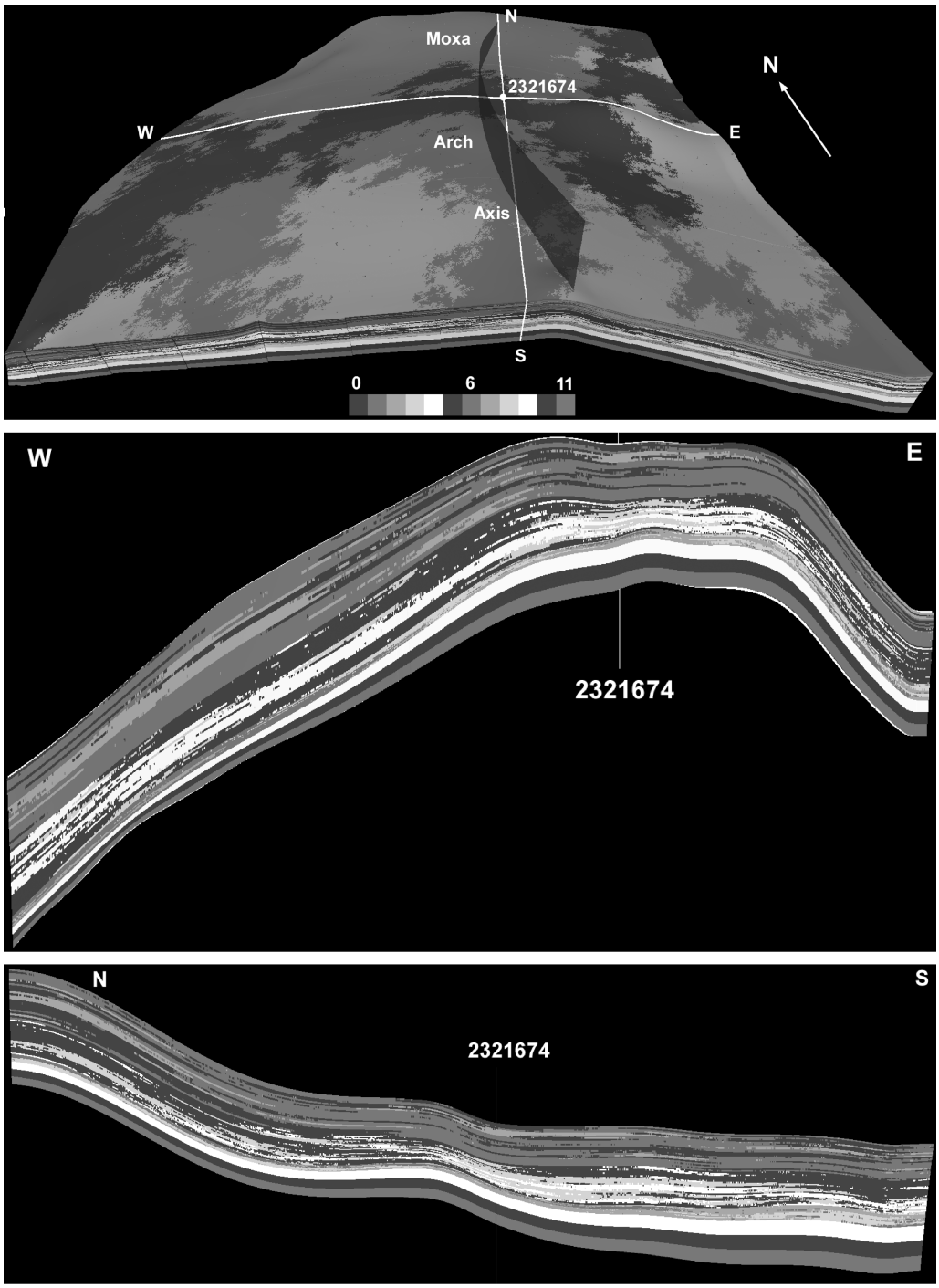

Figure 7. Regional geostatistical facies model in three-dimensional (3-D) and cross sectional views. Vertical exaggeration is 5× (3-D), 17× (east-west transect), and 13× (north-south transect). Location of the transects is indicated in the 3-D view. The transects intersect at the Shute Creek injection well (API: 2321674).

extent is much smaller than its lateral extent. This is qualitatively consistent with the observed facies continuity from well logs, prior observations in the overthrust belt, and Nugget outcrops observed in the northern GRB. Moreover, based on ϕ_{well} separated into the 12 units, a mean ϕ can be estimated for each unit (in percentage; group and facies ID in parentheses): 5.5 (Twin Creek; 0), 8.6 (Twin Creek; 1), 4.5 (Twin Creek; 2), 14.1 (upper Nugget; 3), 13.6 (upper Nugget; 4), 13.1 (upper Nugget; 5), 25.8 (lower Nugget; 6), 3.8 (lower Nugget; 7), 8.1 (lower Nugget; 8), 1.7 (upper Ankareh; 9), 3.1 (middle Ankareh; 10); 3.1 (lower Ankareh; 11).

The upper Nugget group (facies 3–5) has the best overall reservoir quality and is laterally extensive, confirming the original choice of the Nugget

Table 1. Porosity Variogram Parameters of the Nugget Storage Suite

Porosity Groups*	a_h^{max}**	Azimuth** (°)	a_h^{min}**	a_v**	C_0**
Twin Creek group: unit ID = 0–2	85,450	40	63,900	89	0.04
Upper Nugget group: unit ID = 3–5	56,657	40	49,677	132	0.4
Lower Nugget group: unit ID = 6–8	86,657	40	59,677	132	0.3
Upper Ankareh unit: unit ID = 9–10	65,000	40	40,000	90	0.05
Lower Ankareh unit: unit ID = 11	33,207	10	22,192	100	0.1

*Porosity modeling is conducted for five groups: Twin Creek group, upper Nugget group, lower Nugget group, upper Ankareh unit, and lower Ankareh unit.
**a_h^{max} = maximum horizontal correlation range (ft); a_h^{min} = minimum horizontal correlation range (ft); a_v = vertical correlation range (ft); azimuth = major horizontal statistical axis of correlation in relation to north; minor horizontal axis = 90° from azimuth; vertical statistical axis = normal to the horizontal plane; C_0 = the modeled variogram nugget effect.

as a target for gas disposal. Although the highest average ϕ belongs to facies 6 of the lower Nugget, this unit is proportionally small. The lower Nugget is dominated by low-ϕ facies, particularly in southern Moxa arch, where facies 7 and 8 thicken. Compared with the upper Nugget, the Twin Creek facies are of lower reservoir quality, although their total rock volumes are similar. Given that the Twin Creek ϕ is about one-third to one-half of the Nugget ϕ, this formation can still provide significant PV. Locally, the injector at Shute Creek (2321674) penetrates the good-quality laterally continuous Nugget facies, ensuring injectivity. Regionally, the arch structure provides a structural trap for gas (recall that cap rocks exist further above the NSS). The gentle rise toward the north will also influence gas flow; under buoyancy, a northern migration of the injected gas is likely (see Acid Gas Simulation section).

Several points must be noted in facies modeling. The Moxa arch NSS are deep saline aquifers with limited data. Much of the previous sedimentologic information describing these formations pertains to the overthrust belt and thus cannot be used to describe the model, nor be directly compared with it. Second, SIS was used in facies modeling instead of indicator kriging; a simulation-based approach is recommended in reservoir modeling because it can capture small-scale variabilities better than kriging (Deutsch, 2002). Although SIS is considered a good choice in modeling a variety of geologic facies in situations where facies geometric parameters cannot be reliably inferred for object-based methods (Deutsch, 2002; Ma et al., 2009), a set of subjective decisions has been made in selecting variogram models and fitting their parameters. Although SIS is a popular facies modeling method, without detailed and site-specific studies (e.g., those aimed at mapping facies shape, proportion, and juxtaposition relations), the validity of using this versus other techniques cannot be verified (Falivene et al., 2006). In this study, the uncertainty in geostatistical facies modeling is not evaluated because constraints needed for such an analysis are not available. Such constraints can include, for example, facies parameters obtained from outcrop or seismic analysis (Milliken et al., 2008; Sech et al., 2009) or facies probability cubes developed from integrating well data with depositional analyses (Ma, 2009a).

Furthermore, a change-of-support issue arises in facies modeling. Facies heterogeneity is resolved from a cutoff scale (25 ft [7.6 m] in the vertical) and above, instead of from well-log (0.25–1 ft [0.08–0.3 m]) or core scales, reflecting a universal limitation in modeling large reservoirs (Dubois et al., 2006). Before facies modeling, well-log–scale facies types were upscaled to the geostatistical grid cell using the most abundant code (Schlumberger, 2010b). At each well, this method maps the fine-scale facies types to the coarser grid cells by selecting the most volumetrically abundant facies at the subgrid level. The method was found to be reasonably accurate, that is, fine-scale facies proportions are generally preserved at the grid scale. However, for thin facies separated by thick units, the associated upscaled (thin facies) types were generally underestimated. Alternatives to this method also exist, but all suffer issues with sampling bias

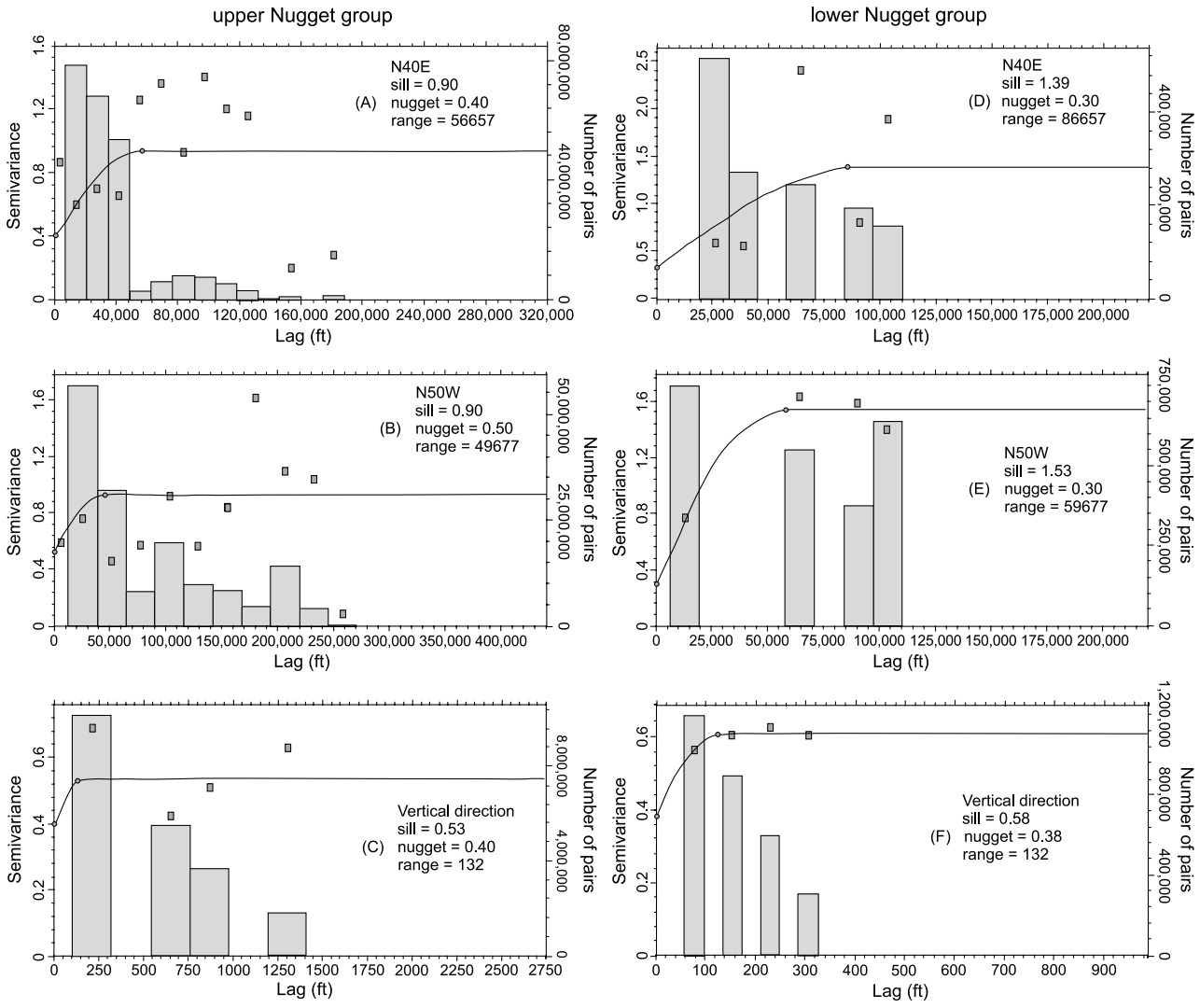

Figure 8. Directional porosity variograms for the upper Nugget (left column) and lower Nugget (right column) groups. Square = experimental variogram; line = fitted model (circles indicate the range and nugget fitted); bar = number of data pairs used in computing each experimental variogram; sill = variogram value at the plateau of the variogram model (i.e., the semivariance value where no correlation exists anymore between pairs of data values); nugget = discontinuity and/or error at the origin of a variogram model (i.e., the vertical distance between 0 and where the variogram model crosses the *y* axis); range = lag distance where the variogram model reaches its plateau (i.e., the separation distance where no correlation exists anymore between pairs of data values).

(Ma, 2009b). In this study, variogram analysis was conducted with the upscaled facies types at wells; during SIS, conditioning at wells was also provided by the upscaled facies. Using the same grid, ϕ upscaling is conducted before its geostatistical modeling—ϕ at the grid cell is obtained from averaging subgrid well-log–scale porosities.

Porosity and Permeability Modeling

Porosity is modeled for each facies using geostatistics. For the Nugget, well-log–derived ϕ_{well} was corrected based on core measurements (but raw ϕ_{well} was used for the Twin Creek and the Ankareh). The ϕ_{well} was then upscaled to the geostatistical (facies) grid. Porosity data were initially divided into the 12 units. For each unit, a mean ϕ is obtained (as discussed above). However, experimental ϕ variograms constructed for each unit exhibited large fluctuations, indicating insufficient sample support. To reduce the artifacts, ϕ from different units was pooled and experimental variograms were recomputed. After trial and error, relatively stable

variograms were achieved with five ϕ groups (Table 1), corresponding to either formation or facies groups. Each group exhibits a distinct mean ϕ, satisfying stationarity assumption in ϕ modeling.

For each ϕ group, experimental variograms were computed with the upscaled ϕ_{well} (Figure 8). Directional spherical models were fitted from which ϕ correlation ranges were obtained. Along the horizontal plane, selection of major and minor statistical axes of correlation was based on the same angles chosen for facies modeling. Stationary functions were selected to model the variograms because an a priori trend analysis did not identify significant ϕ trends. Using the variogram model and histogram, ϕ was populated in each group using the sequential Gaussian simulation (SGS) conditioned to well data. Despite ϕ grouping, SGS was conducted for each of the 12 units. For example, a ϕ variogram and histogram of the Twin Creek Group were used to populate ϕ in each Twin Creek facies (ID = 0–2). Although these facies share the same univariate and bivariate ϕ statistics, ϕ distribution in the reservoir model was controlled by facies and locally conditioned by (within-facies) well data.

The SGS was repeated for the NSS using different random seeds to create 200 ϕ realizations. The number of realizations is case dependent and can vary with data variability and the type of uncertainty measure (Deutsch, 2002). For ranking studies, 200 is deemed sufficiently large (McLennan and Deutsch, 2005). A PV was computed for each realization. To reduce the number of simulation models, three ϕ realizations were selected with P10, P50, and P90 PVs. Next, using the ϕ-$\log_{10}k_h$ transform obtained from core data, three k_h fields were populated, corresponding to the three ϕ realizations. Realization with a higher PV will have a ϕ distribution shifted toward higher values, which translates to a higher k_h distribution. The transform was developed only for the Nugget but was used in populating all formations. A single k_v/k_h was assigned to all formations as well, although this ratio is varied in the sensitivity study to evaluate the influence of fractures on flow. Finally, a local petrophysical model surrounding Shute Creek is extracted from the regional model (Figure 1). This model contains 3,725,568 grid cells for which the P50 ϕ field is shown for each ϕ group (Figure 9). The upper and middle Ankareh units are shown separately. Although variogram analysis was conducted with the ϕ of the upper Ankareh group, SGS results reflect the effect of facies-specific modeling and local well conditioning.

Fluid-Flow Simulation

Simulation Grid

In gas disposal studies, a long simulation time is desired to understand gas migration and trapping in storage formations (Korre et al., 2009). However, with a 3-D model, the cost of simulating multiphase fluid flow with multiple species for a long period is high. Petrophysical properties of the local model (i.e., P10, P50, P90 models) were averaged or upscaled to a coarsened simulation grid (flow grid). To determine appropriate cell spacings for the flow grid, a grid resolution study was conducted using k upscaling (Wen and Gomez-Hernandez, 1996; Renard and de Marsily, 1997). In the analysis, the P50 model was used and k_v/k_h was assigned 1.0 (results of the other models and/or different k_v/k_h are expected to be similar). From the fine grid (horizontal and vertical cell spacing of ~200 ft [~61 m] and ~25 ft [7.6 m], respectively), increasingly coarsened grids were built while honoring formation contacts. These grids have increasing horizontal spacings of approximately 300, 400, 500, 600, and 700 ft (~90, 120, 150, 180, and 210 m, respectively) and a vertical spacing approximately 50 ft (~15 m). The coarsening ratios, up to four times in the horizontal and two times in the vertical, are consistent with those of a modeling study of the Nugget Sandstone in the overthrust belt (Cox et al., 1994). In each coarse grid, a cell ϕ was computed with volume-weighted arithmetic averaging of subgrid ϕ (Schlumberger, 2010a). A cell k was computed by conducting single-phase (water) steady-state flow simulations with the fine grid. Because heterogeneity of the fine grid is dominated by lateral stratification, a diagonal tensor upscaling technique was used (i.e., along every two opposing cell faces, no-flow and linear-potential-drop boundary conditions were assigned to compute three upscaled k components). To enhance the

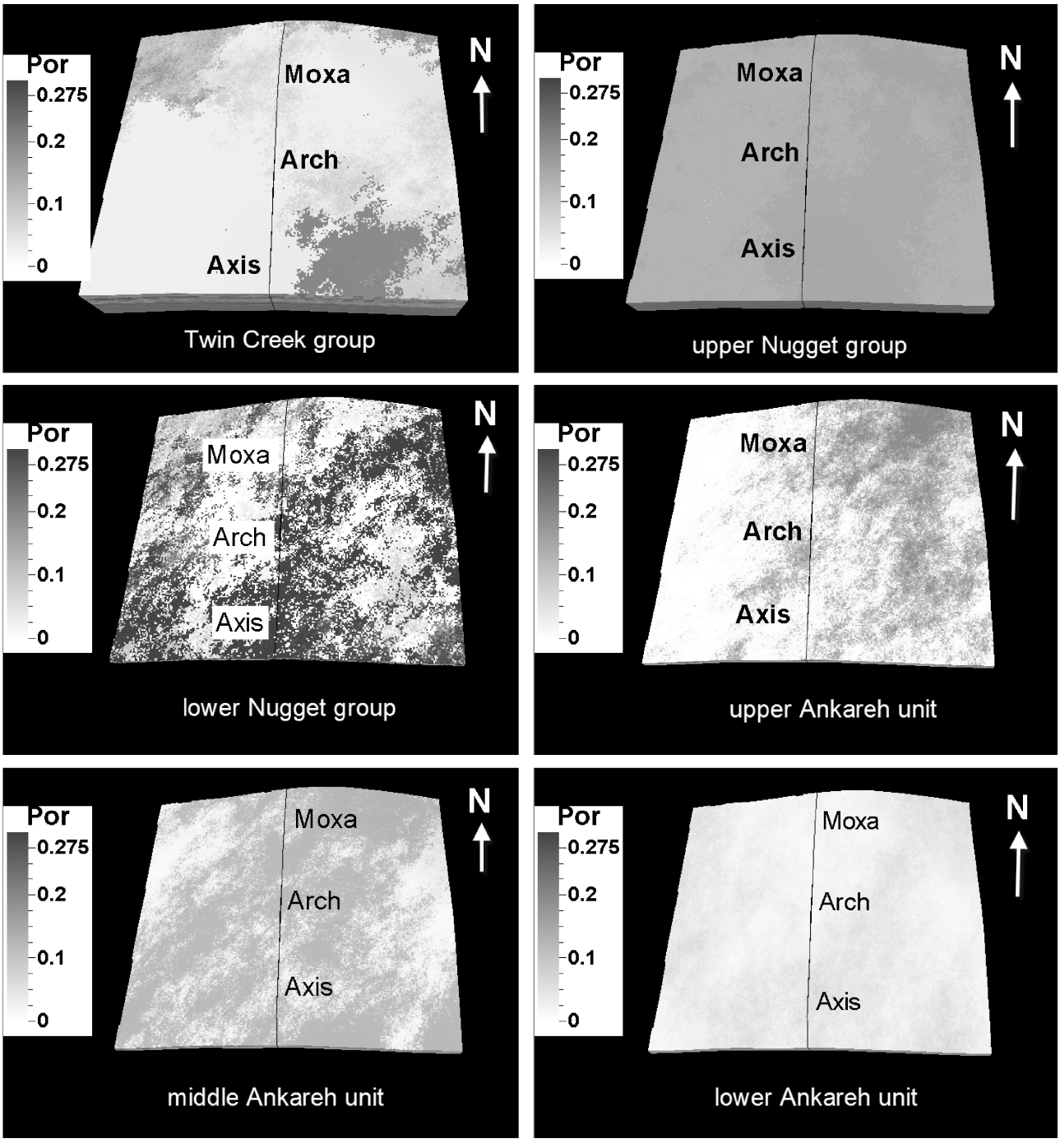

Figure 9. Local model showing the P50 porosity (Por) field before grid coarsening; 5× vertical exaggeration. The Upper Ankareh unit (ID = 9) and Lower Ankareh unit (ID = 10) belong to the Upper Ankareh Group.

accuracy of upscaling, a local method with three skins was used (Wen et al., 2003).

To determine which coarse grid was sufficient to capture fine-grid flow, single-phase steady-state flow was simulated using all grids. A bulk flow rate across the outflow boundary is determined. By comparing this rate with that of the fine grid, a coarse grid with a horizontal spacing of 600 ft (180 m) was selected, which gave a relative error in global flow rate approximately 10% (Table 2). Although finer grids yield better results, numerical experiments with acid gas modeling took unreasonably long

Table 2. Grid Resolution Study Based on Permeability Upscaling*

Grid Size (ft)	Error with 0 Skin (%)	Error with 1 Skin (%)	Error with 2 Skin (%)	Error with 3 Skin (%)
300	7.70	0.60	0.02	–0.10
400	12.00	4.10	3.3	3.10
500	16.50	8.80	7.60	7.20
600	19.70	12.20	11.00	10.70
700	22.60	15.40	13.80	13.30

*A percent error in global flow rate is estimated based on that computed by the fine grid (horizontal cell spacing, ~200 ft [~60 m]).

time (e.g., more than 3 weeks for a single run). Because higher accuracy is desired near the injection well where gas plume emanates, the 600-ft (180-m) grid is modified by local grid refinement (LGR) near the injector. As indicated by simulations, most of the plume travels through this region where the gas is trapped and dissolved. Near-well LGR will offset the discretization error in the coarsened cells elsewhere. Numerical experiments compared a suite of end-member simulations (defined in the Results), with and without LGR. The average enhancement in flow-rate prediction is 4.70%.

Compositional Modeling of Acid Gas Injection

With the flow grid, acid gas simulation was conducted using GASWAT of Eclipse 300 (Schlumberger, 2010a), a multiphase multispecies compositional simulator. The GASWAT is applicable to modeling geologic storage of CO_2 in aquifers and depleted gas reservoirs. Gas composition, however, is not restricted to CO_2. Other gases and their solubilities in water can be modeled assuming equilibrium partitioning. The GASWAT solves the pressure and molar density of each component. Mole fractions of components in gas (or vapor) and aqueous phases are computed through a flash process. Both phase saturations and aqueous concentrations of gas components can be determined. In this study, acid gas injected into the Nugget consists of five components: CO_2 (75%), N_2 (7%), H_2S (5%), CH_4 (10%), and ethane (3%), reflecting an average waste gas composition at the Moxa arch. Formation water is the sixth component. All components' parameters relevant to simulation were obtained using a fluid property package (Schlumberger, 2010b). As significant salinity is observed in Nugget Formation waters, solubility correction was made to reflect the effect of salinity on reducing aqueous solubilities of the gas components. The effect of salinity on brine density is accounted for by an equation of state. With GASWAT, the temperature of the reservoir can vary with depth, which can affect gas solubility, gas densities, brine densities, and viscosities. An initial temperature field was assigned to the model by interpolating temperature log data.

Because of the importance of relative permeability on gas flow, mobility, and residual trapping, the gas-phase relative permeability (k_{rg}) is of significant interest in disposal studies. In saline aquifers, k_{rg} hysteresis can contribute to significant residual CO_2 trapping (e.g., Ide et al., 2007; Qi et al., 2009). However, experimental data conducted under in-situ conditions with different core lithologies suggest that k_{rg} may not exhibit significant hysteresis, depending on host rock mineralogy, pore-size distribution, and dissolution (Bennion and Bachu, 2005, 2006a, b; Horne, 2008). Using experimental k_{rg} of the Viking Sandstone located in Alberta Basin, Canada, uncertainty in k_{rg} will be evaluated using end-member values. The brine phase is assumed nonhysteretic (i.e., water wet); its end point relative permeability and saturations were taken from the same experiments. Furthermore, although capillary pressure can locally affect gas storage, it is assumed negligible and a single fluid pressure is computed (e.g., Kumar et al., 2004; Nordbotten et al., 2005; Juanes et al., 2006; Obi and Blunt, 2006). During injection, gas flow is controlled by the competition between viscous force, gravity, formation heterogeneity, and fluid mobility. Because gas has a lower density than formation brine, postinjection gas migration tends to be dominated by gravity. The effect of adding capillarity will predict a more smoothed plume front, whereas ignoring capillarity will give a more conservative estimate because its explicit modeling enhances residual trapping.

The initial pressure in the model is hydrostatic. A reference pressure is set as 5701 psi (39,307 kPa) at a depth of 12,900 ft (3932 m), assuming a brine density of 1.02 g/cm^3. Before injection, the model

is equilibrated with the brine phase. During injection, boundary condition is represented by a Carter-Tracy analytical aquifer of a large radius and thickness, which ensures an open boundary, allowing injected gas and formation brine to flow out. For the model's side boundary, this choice in effect reflects the regional extent of the NSS beyond the local model. The model top is open because at Shute Creek, the overlying Stump-Pruess cannot be assumed sealing. The bottom of the Ankareh is also open because it overlies the Triassic Thaynes Formation, which locally contains sandstones (Picard et al., 1969). The Stump-Pruess and the Thaynes are not part of the NSS because virtually no data exist for them at the Moxa arch.

During simulation, one injector at Shute Creek is used (API: 2321674), perforating the Nugget Sandstone. A fixed injection rate of 75,000 MSCF (2,123,763 m^3)/day is used. The injection phase lasts 50 yr, and the reservoir model is monitored for 1950 yr, for a total simulation time of 2000 yr. To prevent geomechanical damage to the storage formations, the injection rate was chosen so that the maximum computed fluid pressure will not exceed 1.8 times the hydrostatic pressure. This fracture gradient was selected based on results of pressure leak-off tests from two wells located near Shute Creek (API: 2321687, 2321674) (Hubbert and Willis, 1957; Matthews and Kelly, 1967; Eaton, 1969). Using this gradient, injector bottom-hole pressure (BHP) constraint is set at 10,260 psi (70,740 Kpa).

Sensitivity Analysis

In this study, we aim to understand the influence of uncertain model parameters on prediction uncertainty. For each of the P10, P50, and P90 models (upscaled from the appropriate fine-grid parameters), a sensitivity analysis (SA) was conducted for which several parameters were varied from those of a base-case simulation. Parameters of the base-case have average or expected values for the storage formations (Table 3), whereas those varied in the SA are constrained by existing data and include the following (Table 4; run 31 is base case): (1) TDS of formation brine, (2) fine-grid k_v/k_h (its impact on gas prediction is reflected by the upscaled k computed for the flow grid), (3) relative permeability hysteresis, and (4) scanning curve interpolation. The TDS can influence gas dissolution in brine, as well as density and viscosity of brine. On the time scale of 1 k.y., it was identified as an important factor influencing CO_2 flow in saline aquifers (Sifuentes et al., 2009). Three k_v/k_h ratios were tested, which led to nine separate k upscalings for the three PV models (in the fine grid, locally, k_h is horizontally isotropic and k_v is determined from k_h using the ratio). For ϕ, three upscalings are needed from the fine-grid ϕ models.

Based on site-specific information, an appropriate range must be chosen for each parameter. In selecting a range for TDS, the observed regional minimum (10,000) and maximum (100,000) TDS values in the GRB were used, when Nugget is buried at more than 12,000 ft (>3660 m). The k_v/k_h range reflects the anisotropy ratios of Nugget cores (2.0 to 0.02), although a scaling issue also exists here in assigning core-scale properties to geostatistical grid cells. However, without detailed subgrid data (e.g., outcrop analogs), this issue cannot be easily resolved. The chosen lower value of k_v/k_h may have underestimated the extent of anisotropy at the grid scale. For example, upscaling of detailed sedimentary facies indicates the effect of horizontal stratification in enhancing k_h and decreasing k_v/k_h (Zhang et al., 2006). Such an effect cannot be determined from core analysis, although the range of

Table 3. Parameters of the Base Case

Parameters*	Value/Status
k_r model	No hysteresis
k_{rw}^{end}	1.0
k_{rg}^{end}	0.44
S_w^{res}	0.25
S_g^{res}	0.0
TDS	50,000
k_v/k_h	0.2
r_i (MSCF/day)	75,000
Initial pressure	Hydrostatic

*k_r = relative permeability; k_{rw}^{end} = end point of the relative permeability of water; k_{rg}^{end} = end point of the gas relative permeability; S_w^{res} = residual saturation of water; S_g^{res} = residual saturation of gas; TDS = total dissolved solids; r_i = injection rate of acid gas.

Table 4. Parameters Varied in the Sensitivity Analysis and Associated Prediction Outcomes at the End of Simulation (P50 model)*

Runs	TDS* (ppm)	k_v/k_h	Hysteresis	Scanning Curve Interpolation	Dissolved Acid Gas LB-M (10^8)	Mobile Acid Gas LB-M (10^9)	Trapped Acid Gas LB-M (10^9)	TIG* LB-M (10^9)	Immobile Acid Gas Ratio* (%)	Mobile Acid Gas Ratio (%)
0	100,000	2.0	Small	Carlson	3.58	1.03	1.98	3.39	69.97	30.35
1	100,000	2.0	Small	Killough	3.68	0.99	2.01	3.39	70.07	29.18
2	100,000	2.0	Small	Jargon	3.91	1.22	1.76	3.39	63.37	35.86
3*	**100,000**	2.0	No		**4.30**	**2.00**	**0.94**	**3.39**	**40.44**	**58.82**
4	100,000	2.0	Large	Carlson	2.99	0.60	2.47	3.39	81.44	17.68
5	100,000	2.0	Large	Killough	3.23	0.43	2.61	3.39	86.47	12.67
6	100,000	2.0	Large	Jargon	3.47	0.60	2.42	3.39	81.58	17.74
7	100,000	0.2	Small	Carlson	3.77	0.86	2.14	3.39	74.24	25.34
8	100,000	0.2	Small	Killough	3.83	0.83	2.17	3.39	75.17	24.40
9	100,000	0.2	Small	Jargon	4.24	1.09	1.86	3.39	67.34	32.23
10	100,000	0.2	No		4.71	1.80	1.10	3.39	46.41	52.95
11	100,000	0.2	Large	Carlson	3.00	0.49	2.58	3.39	84.94	14.55
12	100,000	0.2	Large	Killough	3.28	0.32	2.73	3.39	90.69	9.31
13	100,000	0.2	Large	Jargon	3.68	0.51	2.50	3.39	84.60	14.91
14	100,000	0.02	Small	Carlson	4.11	0.76	2.22	3.40	77.50	22.40
15	100,000	0.02	Small	Killough	4.17	0.72	2.25	3.40	78.46	21.31
16	100,000	0.02	Small	Jargon	4.59	1.00	1.92	3.40	70.03	29.52
17	100,000	0.02	No		5.00	1.69	1.19	3.40	49.83	49.75
18	100,000	0.02	Large	Carlson	3.24	0.43	2.64	3.40	87.12	12.66
19	100,000	0.02	Large	Killough	3.37	0.22	2.84	3.40	93.39	6.33
20	100,000	0.02	Large	Jargon	4.02	0.47	2.52	3.40	85.85	13.92
21	50,000	2.0	Small	Carlson	4.45	1.01	1.90	3.39	69.00	29.88
22	50,000	2.0	Small	Killough	4.56	0.98	1.92	3.39	70.04	28.94
23	50,000	2.0	Small	Jargon	4.84	1.21	1.67	3.39	63.45	35.54
24	50,000	2.0	No		5.28	1.93	0.90	3.39	41.97	57.00
25	50,000	2.0	Large	Carlson	3.73	0.59	2.39	3.39	81.41	17.42
26	50,000	2.0	Large	Killough	4.02	0.43	2.54	3.39	86.57	12.53
27	50,000	2.0	Large	Jargon	4.32	0.61	2.32	3.39	81.11	17.89
28	50,000	0.2	Small	Carlson	4.63	0.84	2.07	3.39	74.55	24.78
29	50,000	0.2	Small	Killough	4.71	0.81	2.10	3.39	75.61	23.78
30	50,000	0.2	Small	Jargon	5.20	1.08	1.78	3.39	67.68	31.67
31	50,000	0.2	No		5.75	1.73	1.06	3.39	48.06	51.09
32	50,000	0.2	Large	Carlson	3.69	0.49	2.51	3.39	84.78	12.53
33	50,000	0.2	Large	Killough	4.04	0.31	2.66	3.39	90.13	9.16
34	50,000	0.2	Large	Jargon	4.54	0.51	2.40	3.39	84.14	15.08
35	50,000	0.02	Small	Carlson	5.05	0.73	2.15	3.40	78.19	21.37
36	50,000	0.02	Small	Killough	5.09	0.70	2.18	3.40	79.07	20.55
37	50,000	0.02	Small	Jargon	5.62	0.99	1.83	3.40	70.46	28.99
38	50,000	0.02	No		6.07	1.63	1.15	3.40	51.56	47.89
39	50,000	0.02	Large	Carlson	3.97	0.42	2.57	3.40	87.45	12.27
40	50,000	0.02	Large	Killough	4.37	0.21	2.73	3.40	93.34	6.27
41	50,000	0.02	Large	Jargon	4.97	0.47	2.42	3.40	85.75	13.89
42	10,000	2.0	Small	Carlson	4.97	1.01	1.84	3.39	68.99	29.80
43	10,000	2.0	Small	Killough	5.09	0.98	1.87	3.39	70.08	28.74
44	10,000	2.0	Small	Jargon	5.39	1.20	1.62	3.39	63.54	35.28
45	10,000	2.0	No		5.87	1.90	0.87	3.39	42.88	55.85

Table 4. Continued

Runs	TDS* (ppm)	k_v/k_h	Hysteresis	Scanning Curve Interpolation	Dissolved Acid Gas LB-M (10^8)	Mobile Acid Gas LB-M (10^9)	Trapped Acid Gas LB-M (10^9)	TIG* LB-M (10^9)	Immobile Acid Gas Ratio* (%)	Mobile Acid Gas Ratio (%)
46	10,000	2.0	Large	Carlson	4.18	0.58	2.36	3.39	81.86	17.06
47	10,000	2.0	Large	Killough	4.49	0.42	2.48	3.39	86.44	12.26
48	10,000	2.0	Large	Jargon	4.82	0.61	2.27	3.39	81.02	17.92
49	10,000	0.2	Small	Carlson	5.13	0.83	2.03	3.39	74.81	24.52
50	10,000	0.2	Small	Killough	5.24	0.80	2.04	3.39	75.59	23.51
51	10,000	0.2	Small	Jargon	5.75	1.07	1.72	3.39	67.72	31.41
52	10,000	0.2	No		6.36	1.71	1.03	3.39	49.02	50.27
53	10,000	0.2	Large	Carlson	4.12	0.49	2.47	3.39	84.87	14.38
54	10,000	0.2	Large	Killough	4.48	0.31	2.61	3.39	90.18	9.13
55	10,000	0.2	Large	Jargon	5.03	0.51	2.36	3.39	84.39	14.88
56	10,000	0.02	Small	Carlson	5.58	0.72	2.11	3.40	78.50	21.11
57	10,000	0.02	Small	Killough	5.64	0.68	2.14	3.40	79.46	20.13
58	10,000	0.02	Small	Jargon	6.22	0.97	1.79	3.40	71.07	28.55
59	10,000	0.02	No		6.70	1.60	1.12	3.40	52.59	47.04
60	10,000	0.02	Large	Carlson	4.44	0.41	2.53	3.40	87.64	12.07
61*	**10,000**	**0.02**	**Large**	**Killough**	**4.85**	**0.21**	**2.69**	**3.40**	**93.55**	**6.27**
62	10,000	0.02	Large	Jargon	5.52	0.47	2.36	3.40	85.83	13.75

*TDS = total dissolved solids; dissolved, mobile, and trapped acid gas = gas in place in the reservoir; LB-M = number of moles of gas (lb-mol), for example, 1 LB-M carbon dioxide weighs 44 lb; TIG = total injected gas that includes gas in place and gas that has flowed out of the model; immobile acid gas ratio = gas storage ratio: (dissolved gas in place + trapped gas in place)/TIG × 100%. The same sensitivity analysis is conducted for the P10 and P90 models (not shown).

**Run 31 = base case; run 3 = worst case with the lowest gas storage ratio (in bold font); run 61 = best case with the highest gas storage ratio (in bold font).

the chosen ratio is comparable to that of Cox et al. (1994).

Three k_{rg} functions were selected from the experimental data, two with hysteresis and one without (Figure 10). All functions use the same critical gas saturation, maximum gas saturation, and relative permeability end points. The only difference lies in the magnitude of residual gas saturation (S_g^{res}). The nonhysteresis model has a S_g^{res} equal to critical gas saturation (drainage and imbibition curves coincide). The hysteresis models use two S_g^{res}: 0.28 (small hysteresis) and 0.48 (large hysteresis), with the latter contributing to more gas trapping during imbibition. Because flow reversal may occur within a grid cell before maximum gas saturation is reached, scanning curves are needed in modeling hysteresis within bounding drainage and imbibition curves. Because few experimental scanning curve data exist for gas-brine systems, three interpolation methods were tested: Carlson, Killough, and Jargon (Carlson, 1981; Killough, 1976; Schlumberger, 2010a). All methods have been found to fit the behavior of hydrocarbon systems, although different methods can lead to differing amounts of trapping.

To understand the sensitivity of prediction to parameter variation, four outcomes are defined at the end of simulation: dissolved gas, mobile gas, trapped gas, and a gas storage ratio (GSR). The GSR is the fraction of total immobile gas (dissolved plus trapped) versus the total injected gas (TIG). Because of the open boundary condition assigned to the model, a small amount of the TIG has flowed out. Among all sensitivity runs, this amount is generally small, typically less than 1% (mole fraction).

ACID GAS SIMULATION

Simulation results pertaining to the P50 model are presented first, before they are compared with those of the P10 and P90 models. For accuracy,

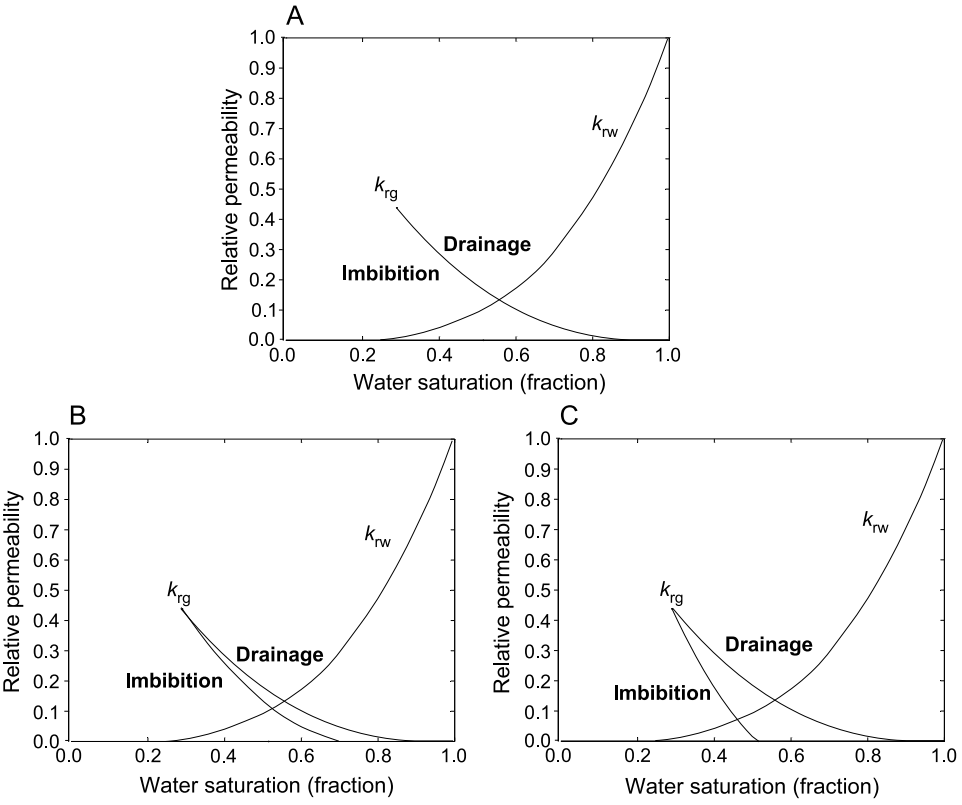

Figure 10. Relative permeability for gas (k_{rg}) and brine (k_{rw}). (A) No hysteresis in k_{rg}. (B) Small hysteresis in k_{rg}. (C) Large hysteresis in k_{rg}. Brine relative permeability is not varied in the sensitivity analysis.

numerical stability was checked for all sensitivity runs. In each run, simulation progress was monitored by checking the time profiles of model outcomes, e.g., mass, pressure, and flow rate. Convergence issues, if they occurred, were previously identified early on and solver parameters were fine tuned whenever appropriate. A few sensitivity runs were rerun after convergence issues developed in later periods. All results were numerically stable solutions of the compositional equations.

Base-Case Simulation

In the base case, at the end of simulation, 48.1% of TIG is stored as dissolved and trapped gas whereas the rest remains mobile. The total gas-phase saturation, including mobile and trapped gas, is plotted along a north-south cross section at the end of the injection and monitoring periods (Figure 11). During injection (Figure 11A), gas flow is dominated by a viscous driving force and gravity, that is, both lateral and vertical migration is observed. During postinjection (Figure 11B), gas flow is dominated by gravity. At the end of simulation, a gas cap has formed beneath the top of the Twin Creek, where a slight updip migration is also observed. Some mobile gas has migrated upward out of the NSS. Because approximately one-half of the TIG is still mobile at this time, this upward migration will continue. Thus, if base-case parameters reflect the condition of the NSS, the sealing capability of the overlying formations needs to be investigated.

By the end of simulation, approximately one-third of the TIG becomes trapped, which is shown as a plume, with lower saturations surrounding the injector (top right). During longer time scales, this trapped gas is expected to dissolve into formation brine until saturation limit is reached. By the end of simulation, approximately 17% of the TIG is dissolved, with a plume shape (not shown) closely resembling the gas-phase plume. During longer time scales, increasing fractions of the TIG will become trapped and dissolved, eventually immobilizing all mobile gas in NSS and overlying formations.

During injection, mobile, trapped, and dissolved gases all increase with time (Figure 11). As gas migrates away from the injector, it becomes trapped

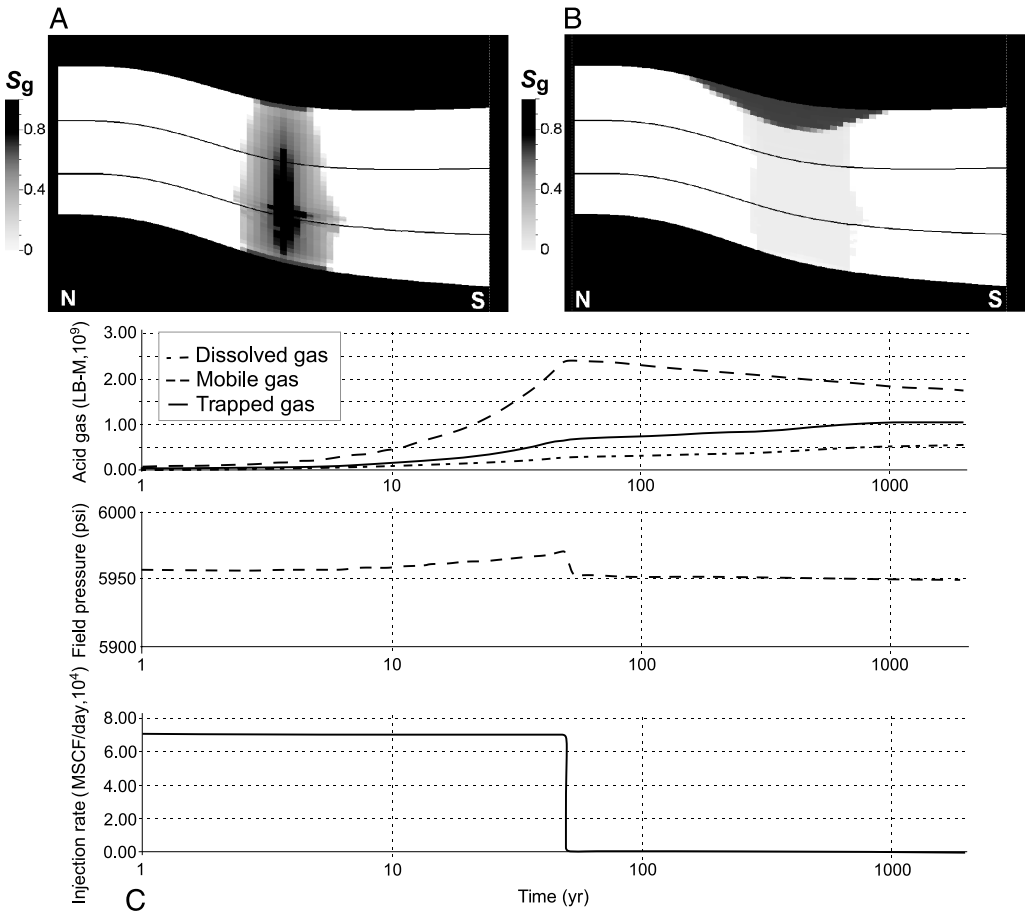

Figure 11. Gas in place predicted by base case (P50 model). (A) Gas-phase saturation (S_g) (mobile plus trapped) at the end of injection along a north-south cross section of the local model. (B) Gas saturation at the end of simulation. In these figures, formation contacts between Twin Creek, Nugget, and Ankareh are shown. The injector is perforated in the Nugget. (C) Time profiles of gas in place, average field pressure, and injection rate. LB-M = number of moles of gas in pounds mole.

in cells when its saturations are below critical gas saturation (i.e., $k_{rg} = 0$). Although this trapping mechanism differs from imbibition-induced residual trapping, a significant amount of gas can be immobilized. This is also observed in other runs when k_{rg} hysteresis was not modeled. After injection ceases, mobile gas decreases, whereas the others increase, as expected. Formation fluid pressure reaches a maximum at the end of injection before declining. Fluid pressure never exceeded the BHP constraint, thus, the injection rate was maintained at a constant value (the simulator will adjust the rate down if fluid pressure exceeds the constraint). This behavior is observed in all sensitivity runs, thus, the TIG is nearly identical for all runs (Table 4), facilitating comparison of the results.

Sensitivity Analysis

Outcomes of the SA are tabulated in Table 4. Runs of particular interest are noted: runs 45 and 19 predict the least and the most amount of trapped gas, respectively; runs 59 and 4 predict the most and the least amount of dissolved gas,respectively; run 61 predicts the highest GSR (best-case scenario); run 3 predicts the most mobile gas, thus, the lowest GSR (worst-case scenario). Below, parameters varied are analyzed to understand their influence on prediction outcomes.

1. With k_{rg} hysteresis, NSS always traps more gas than it does without hysteresis, as expected. At the end of simulation, the average amount of trapped gas from nonhysteresis runs is 1.04×10^9 LB-M (pounds mole), 43.97% smaller than that of the Killough option averaged over the hysteresis runs (2.37×10^9 LB-M).
2. For the hysteresis model with a smaller S_g^{res} (Figure 10B), on average, the Killough option for scanning curve interpolation traps more gas (2.08×10^9 LB-M), followed by Carlson (2.05×10^9 LBM), and Jargon (1.77×10^9 LB-M). The

difference between the most and least trapped gas is 15.98%. For the model with a larger S_g^{res} (Figure 10C), on average, Killough traps 2.65×10^9 LB-M, Carlson 2.50×10^9 LB-M, and Jargon 2.40×10^9 LB-M. The difference between the most and least trapped gas is 10.2%. The variation in the scanning curve interpolation results in a minor to modest variation in the predicted trapped gas.

3. The TDS of formation water strongly influences the amount of dissolved gas. More acid gas is dissolved in brine with a lower salinity. When TDS is 100,000 ppm, the average dissolved gas is 3.82×10^8 LB-M; when it is 10,000 ppm, the average dissolved gas is 5.23×10^8 LB-M. The difference in dissolved gas predicted by these end members is 31.26%.
4. The k_v/k_h also influences the amount of dissolved gas. Comparing run 59 (most dissolved) with run 52 (next to most), the only difference between them is k_v/k_h. As k_v/k_h decreases, more gas is dissolved. The same observation is made comparing run 38 with run 31, and run 17 with run 10. With a lower k_v, the injected gas spreads out more laterally and gas plume contacts more brine, enhancing dissolution. Comparing these same pairs, lower k_v also results in enhanced residual trapping by 8.2 to 8.7%. This is again linked to a larger, more laterally extensive plume conducive to imbibition (Sifuentes et al., 2009). Clearly, nonfractured formations, or formations with high k_h, are preferred for maximizing dissolution and residual trapping (thus storage security), suggesting that fracture characteristics of the NSS should be investigated.

To assess the relative importance of each parameter to the outcomes, the absolute sensitivity measure is computed for each parameter and presented in a sensitivity plot (Figure 12). For the parameters varied, hysteresis (i.e., sensitivity averaged over all scanning curve options) has the greatest impact on nearly all gas forms, followed by k_v/k_h and TDS. This parameter, by exerting the strongest control on the amount of mobile gas (equivalent to total immobile gas because TIG is the same in all runs), also exerts the strongest control on GSR. This

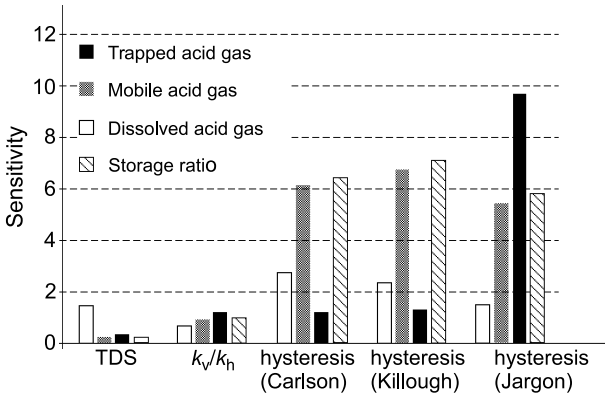

Figure 12. Sensitivity of prediction outcomes at the end of simulation against parameters varied (P50 model). Here, three types of relative permeability scanning curve options are used: Carlson, Killough, and Jargon. TDS = total dissolved solids in brine; k_v/k_h = ratio of vertical permeability to horizontal permeability in grid cells; storage ratio = GSR; dissolved gas = acid gas dissolved into brine, no longer gas phase; mobile gas = acid gas still being gas phase and is mobile; trapped gas = acid gas still in gas phase but no longer migrating.

is consistent with CO_2 modeling results, suggesting that k_{rg} hysteresis exerts a first-order control on gas migration (e.g., Flett and Taggart, 2004; Juanes et al., 2006; Qi et al., 2009). Moreover, when the Jargon option is used, trapped gas is more sensitive to hysteresis than when the other options are used, suggesting that the exact scanning curve needs to be determined if residual gas trapping is to be predicted accurately.

Prediction Range and Uncertainty

If GSR is used as a measure of storage security, among all simulation runs of the P50 model, the worst-case scenario is run 3 with the lowest GSR (40%). The best-case scenario is run 61 with the highest GSR (94%). By comparison, base-case GSR is 48%. Run 3 has the highest TDS, no k_{rg} hysteresis, and the highest k_v/k_h. Gas saturation and profile plots for this run are shown (Figure 13), where a significant gas cap is observed at the end of simulation. Run 61 has the lowest TDS, largest hysteresis, and lowest k_v/k_h. Figure 14 shows its saturation and profile plots. Compared with run 3, the gas cap is much smaller, and more trapped gas is predicted. Comparing gas saturation at the end of simulation (upper right versus middle right), the gas plume

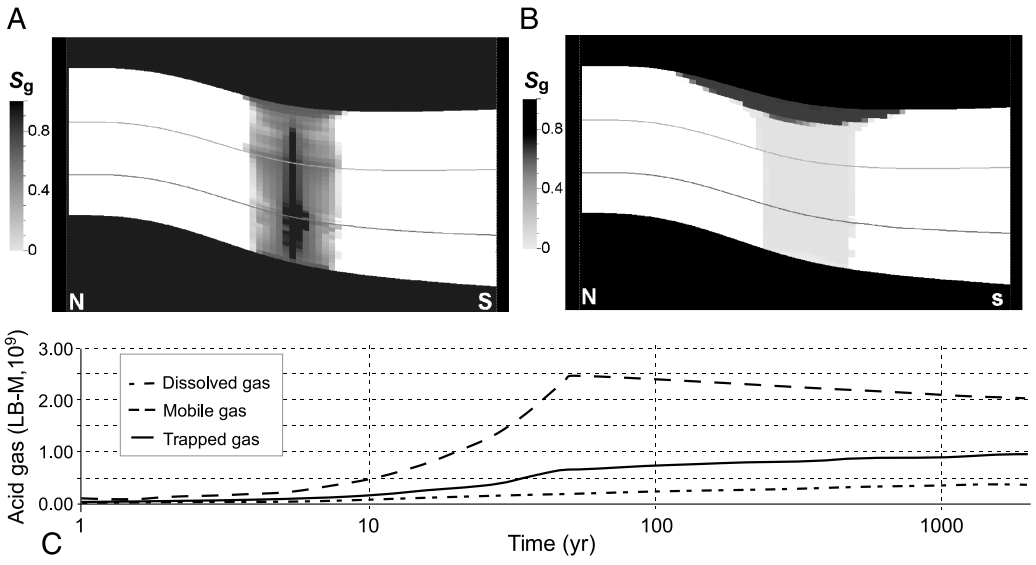

Figure 13. Results of run 3, the worst-case scenario (P50 model). (A) Gas saturation (S_g) (mobile plus trapped) at the end of injection, along the same cross section of Figure 11. (B) Gas saturation at the end of simulation. (C) Time profiles of predicted gas forms. LB-M = pounds mole.

almost entirely consists of trapped gas; this plume will no longer migrate and is effectively immobilized. Furthermore, for all runs with high GSR (above 90%), their parameters share common characteristics: large hysteresis and medium to small k_v/k_h (0.2 and 0.02), whereas all levels of TDS are observed. This confirms the sensitivity result of Figure 12.

For the P50 model, prediction ranges of all gas forms can be estimated. The difference between the maximum and minimum trapped gas is 106%, whereas differences in dissolved and mobile gas are 77 and 162%, respectively. Clearly, given the uncertainty ranges of the parameters, uncertainty increases in predicting dissolved gas, trapped gas, and

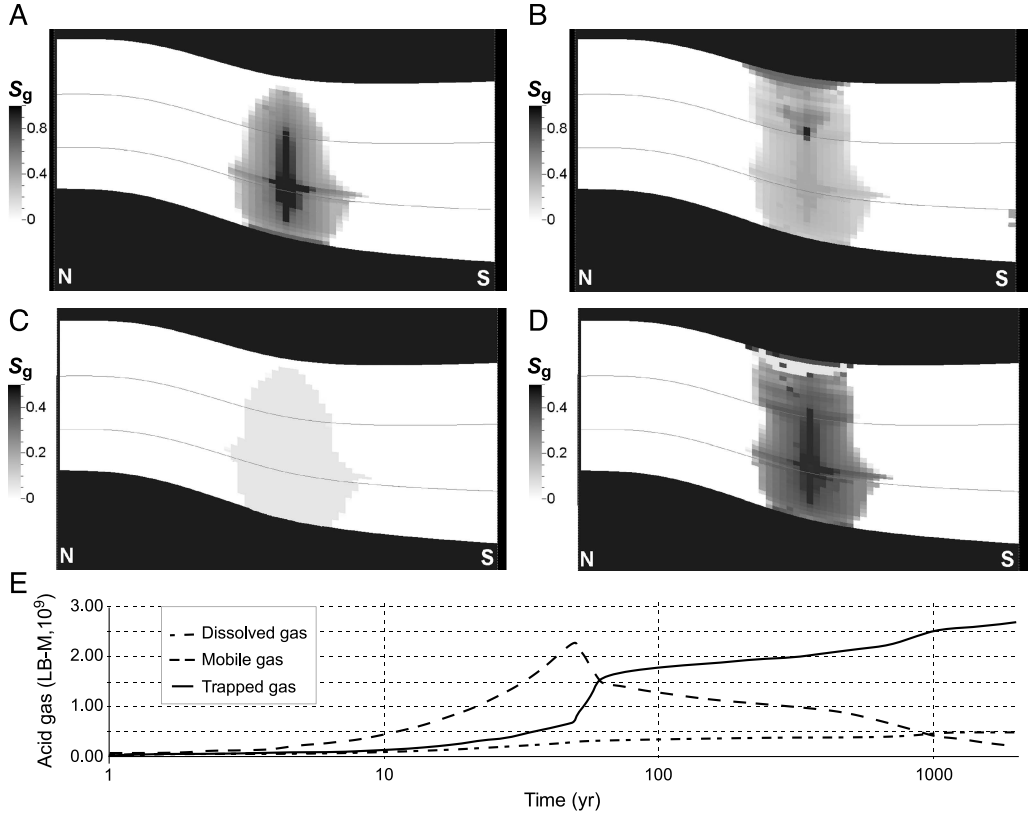

Figure 14. Results of run 61, the best-case scenario (P50 model). (A) Gas saturation (S_g) (mobile plus trapped) at the end of injection. (B) Gas saturation at the end of simulation. (C) Trapped gas saturation at the end of injection. (D) Trapped gas saturation at the end of simulation. (E) Time profiles of predicted gas forms. LB-M = pounds mole.

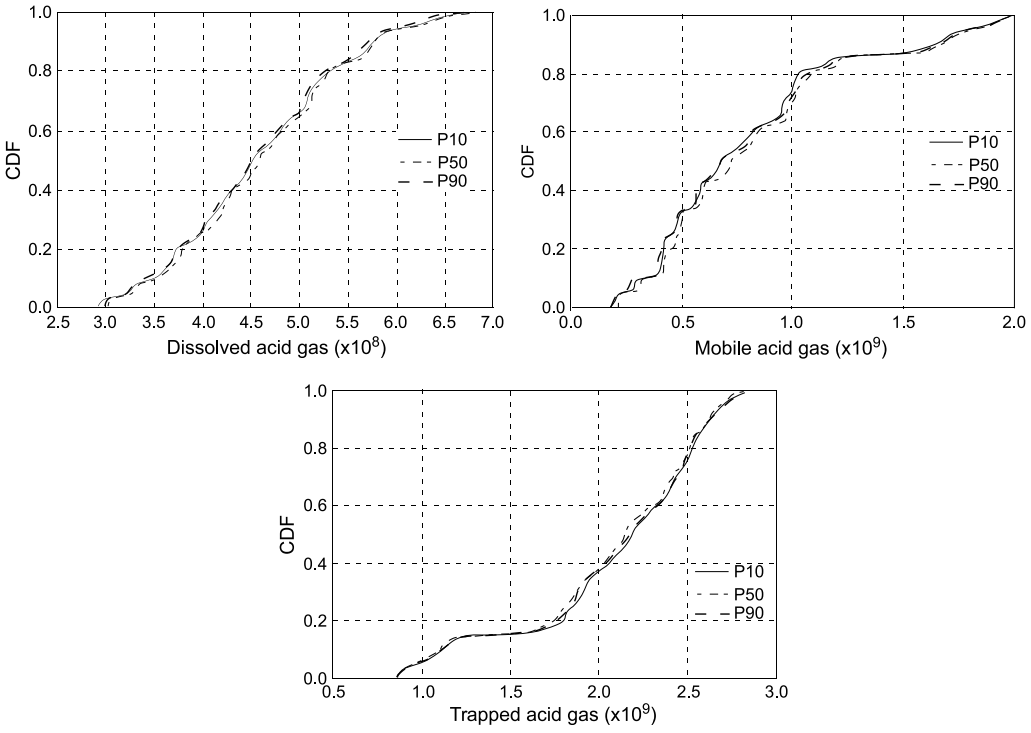

Figure 15. Cumulative distribution for the dissolved, mobile, and trapped acid gas at the end of simulation. CDF = cumulative distribution function.

mobile gas. This suggests that a large variation in prediction outcomes is possible. In particular, the prediction of the mobile gas (thus GSR) is the most variable, and any individual prediction is the least reliable. Mobile gas is also the most sensitive to the parameters varied, whereas dissolved gas is the least sensitive (any individual prediction of this outcome is the most reliable). Reliability in predicting trapped gas lies in the middle.

The effect of petrophysical uncertainty on prediction uncertainty is evaluated by comparing outcomes from the P10, P50, and P90 models. As the same SA is conducted using each model, the outcomes are displayed as cumulative distribution functions of dissolved, mobile, and trapped gases at the end of the simulation period (Figure 15). Under the current modeling assumptions, ϕ and associated k uncertainty exert very minor influences on gas predictions. The P50 model, which represents an average PV, can be reasonably representative of the other models. This result is not surprising because prediction uncertainty arising from a stochastic property model with a fixed structural model and facies distribution is commonly much smaller than those caused by uncertainties in modeling structure and facies as well as in estimating their parameters (e.g., structural fitting coefficients, facies correlation ranges). However, given the computation challenge of gas disposal simulation and current limitations of site data to provide adequate constraints, these uncertainties are not evaluated. Future work will aim to better understand these uncertainties by developing alternative geologic models at the injection site. Results here suggest that, if such uncertainties are unaccounted for, traditional multiple realization approaches in petrophysical modeling may not yield useful estimates on prediction uncertainty.

SUMMARY AND CONCLUSIONS

In this study, acid gas disposal simulation in the Nugget Sandstone of the Moxa arch is of interest. At the regional scale, for the Nugget and its neighboring formations, geologic and engineering data were assembled, screened for accuracy, and digitized, covering an average thickness of approximately 1700 ft (~520 m). Data include wireline logs, core measurements, cross sections, and isopach

maps. They were interpreted and correlated for geologic formations and facies, the latter categorized using Gaussian hierarchical clustering and neural network. Well-log porosities were calibrated with core measurements, whereas a ϕ-$\log_{10}k$ transform was also developed. Using conditional geostatistical simulations (first, sequential indicator simulation of facies, then sequential Gaussian simulation of ϕ), data were integrated at the regional scale to create a fine-grid geostatistical model. Multiple ϕ realizations were created from which models corresponding to P10, P50, and P90 PVs were selected. For the same models, permeabilities were populated using the transform.

To model gas injection, a local model surrounding the injection site was extracted from the regional model and upscaled to a coarsened flow-simulation grid with which multiphase compositional simulations were conducted. A simulation time of 2 k.y. was used with the first 50 yr of the injection phase. With this model, the impact of geologic and engineering variables on acid gas predictions is explored. Results suggest that at the simulation time scale, low TDS, large gas-phase relative permeability hysteresis, and small k_v/k_h all contribute to enhanced gas storage in both residual and dissolved forms. The parameter that exerts the largest control on gas storage is relative permeability hysteresis. Given the uncertain model parameters, the total predicted acid gas storage varies significantly. Prediction uncertainty increases in the order of dissolved gas, trapped gas, and mobile gas. In comparison, petrophysical uncertainty as represented by multiple ϕ realizations has limited impact on prediction, although future work is needed to expand the uncertainty analysis by developing alternative facies models for the storage formations. Future work will also consider modeling reactions of acid gas components with formation brine and minerals. Additional uncertain parameters, for example, reaction paths, mineral surface areas, and kinetic rate constants, will be constrained by laboratory measurements. When field injection occurs at Shute Creek, the model developed in this study will be calibrated against observed pressure and saturation data to further refine its prediction and reduce its uncertainty.

REFERENCES CITED

Bahar, A., and K. Mohan, 1997, Integrated lithofacies and petrophysical properties simulation: Society of Petroleum Engineers Western Regional Meeting, Long Beach, California, June 25–27, 1997, SPE Paper 38261, 6 p.

Bahar, A., and K. Mohan, 2004, Seismic integration for better modeling of rock type based reservoir characterization: A field case example: Abu Dhabi International Petroleum Exhibition and Conference, Abu Dhabi, United Arab Emirates, October 10–13, 2004, SPE Paper 88793, 10 p.

Beaumont, E. A., and N. H. Foster, 1987, Reservoirs I: Properties: AAPG Treatise of Petroleum Geology, Reprint Series 3, 419 p.

Bennion, B., and S. Bachu, 2005, Relative permeability characteristics for supercritical CO_2 displacing water in a variety of potential sequestration zones in the Western Canada sedimentary basin: Society of Petroleum Engineers Annual Technical Conference and Exhibition, Dallas, Texas, October 9–12, 2005, SPE Paper 95547, 15 p.

Bennion, B., and S. Bachu, 2006a, The impact of interfacial tension and pore-size distribution/capillary pressure character on CO_2 relative permeability at reservoir conditions in CO_2-brine systems: Society of Petroleum Engineers/Department of Energy Symposium on Improved Oil Recovery, April 22–26, 2006, Tulsa, Oklahoma, SPE Paper 99325, 10 p.

Bennion, B., and S. Bachu, 2006b, Supercritical CO_2 and H_2S: Brine drainage and imbibitions relative permeability relationships for intergranular sandstone and carbonate formations: Society of Petroleum Engineers of Europec/European Association of Geoscientists and Engineers Annual Conference and Exhibition, Vienna, Austria, June 12–15, 2006, SPE Paper 99326, 13 p.

Brandley, R. T., 1988, Depositional environments of the Triassic Ankareh Formation, Spanish Fork Canyon, Utah: Master's thesis, Brigham Young University, Provo, Utah, 234 p.

Carlson, F. M., 1981, Simulation of relative permeability hysteresis to the nonwetting phase: 56th Annual Fall Technical Conference and Exhibition of Society of Petroleum Engineers of American Institute of Mining Metallurgical and Petroleum Engineers, San Antonio, Texas, October 5–7, 1981, SPE Paper 10157, 9 p.

Cox, D. L., S. J. Lindquist, C. L. Bargas, K. G. Havholm, and R. M. Srivastava, 1994, Integrated modeling for optimum management of a giant gas condensate reservoir, Jurassic eolian Nugget Sandstone, Anschutz Ranch East field, Utah overthrust (U.S.A.): Stochastic modeling and geostatistics: AAPG Computer Applications in Geology, v. 3, p. 287–321.

David, W. S., W. R. Sacrison, and R. C. Hanson, 1975, Structure history of southwestern Wyoming as evidenced from outcrop and seismic: Seismic cross section—AA′ along Moxa arch from south to north, BB′ from west to east over Moxa arch, *in* W. B. Dudley, ed., Symposium on deep drilling frontiers in the Central Rocky Mountains: Denver, Colorado, Rocky Mountain Geological Association, p. 9–20.

Deutsch, C. V., 2002, Geostatistical reservoir modeling, 1st ed.: New York, Oxford University Press, 376 p.

Deutsch, C. V., and A. G. Journel, 1998, GSLIB: Geostatistical software library and user's guide, 2d ed.: New York, Oxford University Press, 369 p.

Dischinger, J. D., and S. Mitra, 2006, Three-dimensional structural model of the Painter and East Painter reservoir structures, Wyoming fold and thrust belt: AAPG Bulletin, v. 90, p. 1171–1185, doi:10.1306/02280605094.

Doelger, N. M., 1987, The stratigraphy of the Nugget Sandstone: The thrust belt revisited: Wyoming Geological Association 38th Annual Field Conference Guidebook, p. 163–178.

Dubois, M. K., G. C. Bohling, and A. P. Byrnes, 2006, Hugoton Asset Management Project: Hugoton geomodel annual report—Static reservoir model: Kansas Geological Survey Open-File Report 2007-6, 53 p.

Eaton, B. A., 1969, Fracture gradient prediction and its application in oil field operations: Journal of Petroleum Technology, v. 42, p. 1353–1360.

Falivene, O., P. Arbues, A. Gardiner, G. Pickup, J. A. Munoz, and L. Cabrera, 2006, Best practice stochastic facies modeling from a channel-fill turbidite sandstone analog (the quarry outcrop), Eocene Ainsa Basin, northern Spain: AAPG Bulletin, v. 90, p. 1003–1029, doi:10.1306/02070605112.

Flett, M. G. R., and I. Taggart, 2004, The function of gas-water relative permeability hysteresis in the sequestration of carbon dioxide in saline formations: Society of Petroleum Engineers Asia Pacific Oil and Gas Conference and Exhibition, Perth, Australia, October 18–20, 2004, SPE Paper 88485, 11 p.

Fraley, C., 1998, Algorithms for model-based Gaussian hierarchical clustering: Society for Industrial and Applied Mathematics Journal on Scientific Computing, v. 20, p. 270–281.

Frost, C. D., 2011, Final report: Carbon sequestration monitoring activities—Department of Energy agreement no. DE-NT0004730: Laramie, Wyoming, University of Wyoming, Office of Research and Economic Development, 318 p.

George, N. P., 1979, Lithology and subdivisions of the Jurassic Stump Formation in southeastern Idaho and adjacent areas: Washington, U.S. Geological Survey, U.S. Geological Survey Professional Paper 1035-C, 25 p.

Gringarten, E., and C. V. Deutsch, 1999, Methodology for variogram interpretation and modeling for improved reservoir characterization: Society of Petroleum Engineers Annual Technical Conference and Exhibition, Houston, Texas, October 3–6, 1999, SPE Paper 56654, 13 p.

Harstad, H., L. W. Teufel, J. C. Lorenz, and S. R. Brown, 1996, Characterization and fluid-flow simulation of naturally fractured Frontier Sandstone, Green River Basin, Wyoming: New Mexico, Albuquerque, Sandia National Laboratories, v. 96-1955, 70 p.

Hilman, M. E., 1973, Stratigraphy and paleoenvironmental analysis of the Upper Jurassic Preuss and Stump formations, western Wyoming and southeastern Idaho: Ph.D. thesis, University of Michigan, Ann Arbor, Michigan, 297 p.

Horne, R. N., 2008, Physical modeling of CO_2 sequestration: Public Interest Energy Research Final Project Report: Stanford, Stanford University, CEC-500-2007-113, 31 p.

Huang, N. S., G. E. Aho, B. H. Baker, T. R. Matthews, and R. J. Pottorf, 2007, Integrated reservoir modeling to maximize the value of a large sour-gas field with high concentrations of inerts: International Petroleum Technology Conference, Dubai, United Arab Emirates, December 4–6, 2007, IPTC Paper 11202, 16 p.

Hubbert, M. K., and D. G. Willis, 1957, Mechanics of hydraulic fracturing: Transactions of the American Institute of Mining Metallurgical and Petroleum Engineers, v. 210, p. 153–166.

Ide, S. T., K. Jessen, and F. M. Orr Jr., 2007, Storage of CO_2 in saline aquifers: Effects of gravity, viscous, and capillary forces on amount and timing of trapping: International Journal of Greenhouse Gas Control, v. 1, p. 481–491, doi:10.1016/S1750-5836(07)00091-6.

Imlay, R. W., 1950, Jurassic rocks in the mountains along the west side of the Green River Basin: Wyoming Geological Association, Fifth Annual Field Conference, Southwestern Wyoming Guidebook, August 8–11, 1950: Casper, Kintzel Blue Print Company, p. 37–49.

Jensen, P. H., 2005, Mapping and piecing together the Triassic/Jurassic stratigraphy along the south flank of the Uinta Mountains, northeast Utah: A stratigraphic analysis of the Bell Springs Member of the Nugget Sandstone: Master's thesis, Brigham Young University, Provo, Utah, 59 p.

Juanes, R., E. J. Spiteri, F. M. Orr, Jr., and M. J. Blunt, 2006, Impact of relative permeability hysteresis on geological CO_2 storage: Water Resources Research, v. 42, 13 p., doi:10.1029/2005WR004806.

Killough, J. E., 1976, Reservoir simulation with history-dependent saturation functions: Society of Petroleum Engineers Journal, v. 16, p. 37–48.

Knapp, R. R., 1978, Depositional environments and diagenesis of the Nugget Sandstone: South-central Wyoming, northeast Utah and northwest Colorado: Wyoming Geological Association, Resources of the Wind River Basin 30th Annual Field Conference Guidebook, p. 131–138.

Korre, A., J. Q. Shi, C. Imrie, and S. Durucan, 2009, Modeling the uncertainty and risks associated with the design and life cycle of CO_2 storage in coal-bed reservoir: Energy Procedia, v. 1, p. 2525–2532, doi:10.1016/j.egypro.2009.02.016.

Krystinik, L. F., 2000, Predicting fractures 5 km down: Integrated reservoir characterization—Union Pacific Resources/Department of Energy Rock Island 4-H well (abs.): AAPG Bulletin, v. 84, p. 1878.

Kumar, A., M. Noh, G. A. Pope, K. Sepehrnoori, S. Bryant, and L. W. Lake, 2004, Reservoir simulation of CO_2 storage in deep saline aquifers: Society of Petroleum Engineers/Department of Energy 14th Symposium on Improved Oil Recovery, Tulsa, Oklahoma, April 17–21, 2004, SPE Paper 89343, 10 p.

Lamerson, P. R., 1982, The Fossil Basin and its relationship to the Absaroka thrust system, Wyoming and Utah, *in* R. B.

Powers, ed., Geological studies of the Cordilleran thrust belt: Denver, Colorado, Rocky Mountain Association of Geologists, v. 1, p. 279–340.
Lander, R. H., and O. Walderhaug, 1999, Predicting porosity through simulating sandstone compaction and quartz cementation: AAPG Bulletin, v. 83, no. 3, p. 433–449.
Lewis, H., and G. D. Couples, 1993, Production evidence for geological heterogeneities in the Anschutz Ranch East field, western U.S.A., *in* C. P. North and D. J. Prosser, eds., Characterization of fluvial and eolian reservoirs: Geological Society (London) Special Publication 73, p. 321–338.
Lindquist, S. J., 1983, Nugget Formation reservoir characteristics affecting production in the overthrust belt of southwestern Wyoming: Journal of Petroleum Technology, v. 35, p. 1355–1365.
Lorenz, J. C., 1995, Recognition and use of induced fractures, and other features in core produced by the coring processing (abs.): New Mexico, Albuquerque, Sandia National Laboratories, 11 p.
Love, J. D., and A. C. Christiansen, 1985, Geologic map of Wyoming: U.S. Geological Survey, scale 1:500,000, 3 sheets.
Lynds, R., E. Campbell-Stone, T. P. Becker, and C. Frost, 2010, Stratigraphic evaluation of reservoir and seal in a natural CO_2 field: Lower Paleozoic, Moxa arch, southwest Wyoming: Rocky Mountain Geology, v. 45, p. 113–132, doi:10.2113/gsrocky.45.2.113.
Ma, Y. Z., 2009a, Propensity and probability in depositional facies: Mathematical Geosciences, v. 41, p. 737–760, doi:10.1007/s11004-009-9239-z.
Ma, Y. Z., 2009b, Simpson's paradox in natural resource evaluation: Mathematical Geosciences, v. 41, p. 193–213, doi:10.1007/s11004-008-9187-z.
Ma, Y. Z., A. Seto, and E. Gomez, 2009, Depositional facies analysis and modeling of the Judy Creek reef complex of the Upper Devonian Swan Hills, Alberta, Canada: AAPG Bulletin, v. 93, p. 1235–1256, doi:10.1306/05220908103.
MacLachlan, M. E., 1972, Triassic System, *in* W. W. Mallory, ed., Geological atlas of the Rocky Mountain region: Denver, Colorado, Rocky Mountain Association of Geologists, p. 166–176.
Matthews, W. R., and J. Kelly, 1967, How to predict formation pressure and fracture gradient: Oil & Gas Journal, v. 65, p. 92–1066.
McLennan, J. A., and C. V. Deutsch, 2005, Ranking geostatistical realizations by measures of connectivity: Society of Petroleum Engineers/Petroleum Society of Canadian Institute of Mining, Metallurgy and Petroleum/Canadian Heavy Oil Association International Thermal Operations and Heavy Oil Symposium, Calgary, Alberta, Canada, November 1–3, 2005, SPE Paper 98168, 13 p.
McLennan, J. A., and C. V. Deutsch, 2006, Best practice reservoir characterization for the Alberta oil sands: Canadian International Petroleum Conference, Calgary, Alberta, Canada, June 13–15, 2006, Society of Petroleum Engineers Paper 2006-096, 4 p.
Melick, J. J., and M. H. Gardner, 2009, Incorporating geologic heterogeneity in 3-D basin-scale models for CO_2 sequestration: Examples from the Powder River Basin, northeast Wyoming and southeast Montana: Society of Petroleum Engineers International Conference on Carbon Dioxide Capture, Storage and Utilization, San Diego, California, November 2–4, 2009, SPE Paper 126443, 22 p.
Milliken, W. J., M. Levy, S. Strebelle, and Y. Zhang, 2008, The effect of geologic parameters and uncertainties on subsurface flow: Deep-water depositional systems: Society of Petroleum Engineers Western Regional and Pacific Section AAPG Joint Meeting, Bakersfield, California, March 31–April 2, 2008, SPE Paper 114099, 16 p.
Morad, S., K. Al-Ramadan, J. M. Ketzer, and L. F. De Ros, 2010, The impact of diagenesis on the heterogeneity of sandstone reservoirs: A review of the role of depositional facies and sequence stratigraphy: AAPG Bulletin, v. 94, p. 1267–1309, doi:10.1306/04211009178.
Nelson, R. A., 2001, Geological analysis of naturally fractured reservoirs, 2d ed.: Boston, Gulf Professional Publishing, 332 p.
Nordbotten, J. M., M. A. Celia, and S. Bachu, 2005, Injection and storage of carbon dioxide in deep saline aquifers: Analytical solution for carbon dioxide plume evolution during injection: Transport in Porous Media, v. 58, p. 339–360, doi:10.1007/s11242-004-0670-9.
Obi, E., and M. J. Blunt, 2006, Streamline-based simulation of carbon dioxide storage in a North Sea aquifer: Water Resources Research, v. 42, p. 1–13, doi:10.1029/2004WR003347.
Pacht, J. A., 1977, Diagenesis of the Nugget sandstone: Western Wyoming and north-central Utah: 29th Annual Field Conference, Wyoming Geological Association Guidebook, p. 207–219.
Peterson, J. A., 1955, Marine Jurassic rocks, northern and eastern Uinta Mountains and adjacent areas: Tenth Annual Field Conference, Wyoming Geological Association Guidebook, p. 75–79.
Peterson, J. A., 1972, Triassic System, *in* W. W. Mallory, Geological atlas of the Rocky Mountain region: Rocky Mountain Association of Geologists, p. 177–189.
Picard, D. M., 1975, Facies, petrography and petroleum potential of Nugget Sandstone (Jurassic), southwestern Wyoming and northeastern Utah, *in* D. W. Bolyard, ed., Symposium on deep drilling frontiers of the central Rocky Mountains: Rocky Mountain Association of Geologists Guidebook, p. 109–127.
Picard, D. M., 1977, Petrology of the Jurassic Nugget Sandstone, northeast Utah and southwest Wyoming, *in* E. L. Heisey, D. E. Lawson, E. R. Norwood, P. H. Wach, L. A. Hale, eds., Rocky Mountain thrust belt geology and resources: 29th Annual Field Conference, Wyoming Geological Association Guidebook 29, p. 239–258.
Picard, M. D., R. Aadland, and R. Lee, 1969, Correlation and stratigraphy of Triassic Red Peak and Thaynes formations, western Wyoming and adjacent Idaho: AAPG Bulletin, v. 53, p. 2274–2289.
Qi, R., T. C. LaForce, and M. J. Blunt, 2009, Design of carbon dioxide storage in aquifers: International Journal of Greenhouse Gas Control, v. 3, p. 195–205, doi:10.1016/j.ijggc.2008.08.004.
Renard, P., and G. de Marsily, 1997, Calculating equivalent

permeability: A review: Advances in Water Resources, v. 20, p. 253–278, doi:10.1016/S0309-1708(96)00050-4.
Royse, F., 1993, An overview of the geological structure of the thrust belt in Wyoming, northern Utah and eastern Idaho, *in* A. W. Snoke, ed., Geology of Wyoming: Geological Survey of Wyoming Memoir 5, p. 273–311.
Royse Jr., F., M. A. Warner, and D. L. Reese, 1975, Thrust belt structural geometry and related stratigraphic problems, Wyoming-Idaho-northern Utah, *in* D. W. Bolyar, ed., Symposium on deep drilling frontiers in the central Rocky Mountains: Rocky Mountain Association of Petroleum Geologists, p. 41–54
Schlumberger, 2010a, Eclipse technical description manual: Abingdon, United Kingdom, Schlumberger Inc, 1760 p.
Schlumberger, 2010b, Petrel technical description manual: Abingdon, United Kingdom, Schlumberger Inc, 3417 p.
Sech, R. P., M. D. Jackson, and G. J. Hampson, 2009, Three-dimensional modeling of a shoreface-shelf parasequence reservoir analog: Part 1. Surface-based modeling to capture high-resolution facies architecture: AAPG Bulletin, v. 93, p. 1155–1181, doi:10.1306/05110908144.
Sifuentes, W., B. M. Blunt, and M. A. Giddins, 2009, Modeling carbon dioxide storage in aquifers: Assessing the key contributors to uncertainty: Society of Petroleum Engineers Offshore Europe Oil and Gas Conference and Exhibition, Aberdeen, United Kingdom, September 8–11, 2009, SPE Paper 123582, 13 p.
Spangler, L., 2007, Regional characterization activities and large-volume injection test, Nugget Sandstone Formation: Regional Carbon Sequestration Partnerships Initiative Review Meeting, Pittsburgh, Pennsylvania, December 12, 2007, 26 p.
Weber, K. J., and L. C. van Guens, 1990, Framework for constructing clastic reservoir simulation models: Journal of Petroleum Technology, v. 42, p. 1248–1297.
Wen, X.-H., and J. Gomez-Hernandez, 1996, Upscaling hydraulic conductivities in heterogeneous media: An overview: Journal of Hydrology, v. 183, p. ix–xxxii, doi:10.1016/S0022-1694(96)80030-8.
Wen, X.-H., L. Durlofsky, and M. Edwards, 2003, Use of border regions for improved permeability upscaling: Mathematical Geology, v. 35, p. 521–547, doi:10.1023/A:1026230617943.
Wilkins, S. J., 2007, Fracture intensity from geomechanical models: Application to the Blue Forest 3-D Survey, Green River Basin, Wyoming, U.S.A.: Geological Society (London) Special Publication 292, p. 137–157.
Wyoming Oil Gas Conservation Commission, 2009, Wyoming Oil Gas Conservation Commission Online Well Database: http://wogcc.state.wy.us/ (accessed March 2, 2010).
Zhang, Y., C. W. Gable, and M. Person, 2006, Equivalent hydraulic conductivity of an experimental stratigraphy: Implications for basin-scale flow simulations: Water Resources Research, v. 42, 19 p., doi:10.1029/2005WR004720.